

Review Article

Reactor Neutrinos

Soo-Bong Kim,¹ Thierry Lasserre,² and Yifang Wang³

¹ KNRC, Department of Physics and Astronomy, Seoul National University, Seoul 151-742, Republic of Korea

² CEA, Irfu, SPP, Centre de Saclay, 91191 Gif-sur-Yvette, France and Astroparticule et Cosmologie APC, 10 rue Alice Domon et Léonie Duquet, 75205 Paris Cedex 13, France

³ Institute of High Energy Physics, Yu-Quan road 19B, Beijing 100049, China

Correspondence should be addressed to Yifang Wang; yfwang@ihep.ac.cn

Received 18 August 2012; Accepted 20 December 2012

Academic Editor: Koichiro Nishikawa

Copyright © 2013 Soo-Bong Kim et al. This is an open access article distributed under the Creative Commons Attribution License, which permits unrestricted use, distribution, and reproduction in any medium, provided the original work is properly cited.

We review the status and the results of reactor neutrino experiments. Short-baseline experiments have provided the measurement of the reactor neutrino spectrum, and their interest has been recently revived by the discovery of the reactor antineutrino anomaly, a discrepancy between the reactor neutrino flux state of the art prediction and the measurements at baselines shorter than one kilometer. Middle and long-baseline oscillation experiments at Daya Bay, Double Chooz, and RENO provided very recently the most precise determination of the neutrino mixing angle θ_{13} . This paper provides an overview of the upcoming experiments and of the projects under development, including the determination of the neutrino mass hierarchy and the possible use of neutrinos for society, for nonproliferation of nuclear materials, and geophysics.

1. Introduction: 80 Years of Reactor Neutrino Physics

Invented by Pauli [1] in 1930, named by Amaldi in 1934, and later modeled in the Fermi theory of beta decay [2]. The weakly coupling neutrino was first searched for by Reines and Cowan. Starting at the Hanford nuclear reactor (Washington), they later moved to the new Savannah River Plant (South Carolina) to perform their definitive and groundbreaking experimental detection. This breakthrough had two important consequences: resolving and clarifying the unsatisfactory situation of a fundamental particle needed for the consistency of theory, but first thought to be unobservable, and demonstrating the possibility of using neutrinos as a sensitive probe of particle physics. Indeed, several years after the completion of the pioneering, Reines and Cowan's work neutrinos were beginning to be used regularly to investigate the weak interactions, the structure of nucleons, and the properties of their constituent quarks.

In the first crude experiment of 1953 [3], Reines and Cowan's goal was to demonstrate unambiguously a reaction caused in a target by a neutrino produced elsewhere. The experiment pioneered the delayed coincidence technique to search for the reaction: $\bar{\nu}_e + p \rightarrow e^+ + n$, where an electron

antineutrino from the Hanford nuclear reactor interacted with a free proton in a large tank filled with cadmium-loaded liquid scintillator. The positron and the resultant annihilation gamma rays are detected as a prompt signal, while the neutron is thermalized in the liquid scintillator and subsequently captured by the cadmium. The excited nucleus then emits gamma radiation which is detected as the delayed signal. The first result, at two standard deviations, was followed in 1956 and 1958 by more precise experiments [4–6], where the significance improved to over four standard deviations. In addition to the detection, the reaction cross-section was measured to be $11 \pm 2.6 \times 10^{-44} \text{ cm}^2$ [6]. Nowadays, reactor neutrinos like Daya Bay, KamLAND, or Double Chooz are still detected through similar experimental methods.

2. Nuclear Reactors and Neutrinos

Nuclear reactors are very intense sources of neutrinos that have been used all along the neutrino's history, from its discovery up to the most recent oscillation studies. With an average energy of about 200 MeV released per fission and 6 neutrinos produced along the β -decay chains of the fission

products, one expects about 2×10^{20} ν /s emitted in a 4π solid angle from a 1 GW reactor (thermal power). Since unstable fission products are neutron-rich nuclei, all β decays are of β^- type, and the neutrino flux is actually pure electronic antineutrinos ($\bar{\nu}_e$).

The neutrino oscillation search at a reactor is always based on a disappearance measurement, using the powerful inverse beta decay (IBD) detection process to discriminate the neutrino signal from backgrounds. The observed neutrino spectrum at a distance L from a reactor is compared to the expected spectrum. If a deficit is measured, it can be interpreted in terms of the disappearance probability which, in the two neutrino mixing approximation, reduces to

$$P_{ee} = 1 - \sin^2 2\theta \sin^2 \left(\frac{\Delta m^2 L}{4E} \right), \quad (1)$$

where Δm^2 is the difference between the squared masses of the two neutrino states and θ is the mixing angle fixing the amplitude of the oscillation.

Here, we will especially consider reactor antineutrino detector at short distances below 100 m from the reactor core, in particular ILL-Grenoble, Goesgen, Rovno, Krasnoyarsk, Savannah River, and Bugey [7–15]. These experiments have played an important role in the establishment of neutrino physics, and especially neutrino oscillations, over the last fifty years. Unlike modern long-baseline reactor experiments motivated by the measurement of the last unknown mixing angle θ_{13} [16–18], which measure P_{ee} by comparing the event rate and spectrum in two detectors at different distances, the aforementioned short baseline experiments can only employ one detector and therefore depend on an accurate theoretical prediction for the emitted $\bar{\nu}_e$ flux and spectrum to measure P_{ee} .

Until late 2010, all data from reactor neutrino experiments appeared to be fully consistent with the mixing of ν_e , ν_μ , and ν_τ with three mass eigenstates, ν_1 , ν_2 , and ν_3 , with the squared mass differences $|\Delta m_{31}^2| \simeq 2.4 \cdot 10^{-3} \text{ eV}^2$ and $\Delta m_{21}^2 / |\Delta m_{31}^2| \simeq 0.032$. The measured rate of $\bar{\nu}_e$ was found to be in reasonable agreement with that predicted from the “old” reactor antineutrino spectra [19–21], though slightly lower than expected, with the measured/expected ratio at 0.980 ± 0.024 , including recent revisions of the neutron mean lifetime, $\tau_n = 881.5 \text{ s}$, in 2011 (PDG).

In preparation for the Double Chooz reactor experiment [16], the Saclay reactor neutrino group reevaluated the specific reactor antineutrino flux for ^{235}U , ^{239}Pu , ^{241}Pu , and ^{238}U . In 2011, they reported their results [22], which correspond to a flux that is a few percent higher than the previous prediction. This also necessitates a reanalysis of the ratio of the observed event rate to the predicted rate for 19 published experiments at reactor-detector distances below 100 m.

2.1. Reference Antineutrino Spectra. Fission reactors release about 10^{20} $\bar{\nu}_e$ $\text{GW}^{-1}\text{s}^{-1}$, which mainly come from the beta

decays of the fission products of ^{235}U , ^{238}U , ^{239}Pu , and ^{241}Pu . The emitted antineutrino spectrum is then given by:

$$S_{\text{tot}}(E_\nu) = \sum_k f_k S_k(E_\nu), \quad (2)$$

where f_k refers to the contribution of the main fissile nuclei to the total number of fissions of the k th branch and S_k to their corresponding neutrino spectrum per fission.

The distribution of the fission products of uranium or plutonium isotopes covers hundreds of nuclei, each of them contributing to $S_k(E)$ through various β decay chains. At the end the total antineutrino spectrum is a sum of thousands of β -branches weighted by the branching ratio of each transition and the fission yield of the parent nucleus. Despite the impressive amount of data available in nuclear databases, the *ab initio* calculation of the emitted antineutrino spectrum is difficult. Moreover, when looking at the detected spectrum through the IBD process, the 1.806 MeV threshold and the quadratic energy dependence of the cross-section enhance the contribution of transitions with large endpoints ($E_0 > 4 \text{ MeV}$). Systematic errors of the nuclear data and the contribution of poorly known nuclei become a real limitation for the high energy part of the antineutrino spectrum. Uncertainties below the 10% level seem to be out of reach with the *ab initio* approach, preventing any accurate oscillation analysis.

In order to circumvent this issue, measurements of total β spectra of fissile isotopes were performed in the 1980s at ILL [19–21], a high flux research reactor in Grenoble, France. Thin target foils of fissile isotopes ^{235}U , ^{239}Pu and ^{241}Pu , were exposed to the intense thermal neutron flux of the reactor. A tiny part of the emitted electrons could exit the core through a straight vacuum pipe to be detected by the high resolution magnetic spectrometer BILL [23]. The electron rates were recorded by a pointwise measurement of the spectrum in magnetic field steps of 50 keV, providing an excellent determination of the shape of the electron spectrum with subpercent statistical error. The published data were smoothed over 250 keV. Except for the highest energy bins with poor statistics, the dominant error was the absolute normalization, quoted around 3% (90% CL), with weak energy dependence.

In principle, the conversion of a β -spectrum into an antineutrino spectrum can be done using the energy conservation between the two leptons

$$E_e + E_\nu = E_0, \quad (3)$$

with E_0 , the endpoint of the β transition. However this approach requires to know the contribution of all single branches in the ILL spectra and this information is not accessible from the integral measurement. Therefore a specific conversion procedure was developed using a set of 30 “virtual” β -branches, fitted on the data. The theoretical

expression for the electron spectrum of a virtual branch was of the form

$$S_{\text{virtual}}(Z, A, E_e) = \underbrace{\frac{K}{\text{Norm.}}}_{\text{Norm.}} \times \underbrace{\mathcal{F}(Z, A, E_e)}_{\text{Fermi function}} \times \underbrace{p_e E_e (E_e - E_0)^2}_{\text{Phasespace}} \times \underbrace{(1 + \delta(Z, A, E_e))}_{\text{Correction}}, \quad (4)$$

where Z and A are the charge and atomic number of the parent nucleus and E_0 is the endpoint of the transition. The origin of each term is described by the underbraces. The δ term contains the corrections to the Fermi theory. In the ILL papers, it included the QED radiative corrections as calculated in [24]. The Z dependence comes from the Coulomb corrections. Since a virtual branch is not connected to any real nucleus, the choice of the nuclear charge was described by the observed mean dependence of Z on E_0 in the nuclear databases

$$Z(E_0) = 49.5 - 0.7E_0 - 0.09E_0^2, \quad Z \leq 34. \quad (5)$$

The A dependence is weaker and linked to the determination of Z through global nuclear fits.

Once the sum of the 30 virtual branches is fitted to the electron data, each of them is converted to an antineutrino branch by substituting E_e by $E_0 - E_\nu$ in (4) and applying the correct radiative corrections. The predicted antineutrino spectrum is the sum of all converted branches. At the end of this procedure, an extra correction term is implemented in an effective way as

$$\Delta S_{\text{branch}}(E_\nu) \approx 0.65(E_\nu - 4.00) \%. \quad (6)$$

This term is an approximation of the global effect of weak magnetism correction and finite size Coulomb correction [25].

The final error of the conversion procedure was estimated to be 3-4% (90% CL), to be added in quadrature with the electron calibration error which directly propagates to the antineutrino prediction. From these reference spectra, the expected antineutrino spectrum detected at a reactor can be computed. All experiments performed at reactors since then relied on these reference spectra to compute their predicted antineutrino spectrum.

2.2. New Reference Antineutrino Spectra. Triggered by the need for an accurate prediction of the reactor antineutrino flux for the first phase of the Double Chooz experiment, with a far detector only, the determination of antineutrino reference spectra has been revisited lately [22]. In a first attempt, a compilation of the most recent nuclear data was performed for an up-to-date *ab initio* calculation of the antineutrino fission spectra. The asset of this approach is the knowledge of each individual β branch, providing a perfect control of the conversion between electron and antineutrino spectra. As a powerful cross-check, the sum of all the branches must match the very accurate electron spectra measured at ILL. Despite the tremendous amount of nuclear data available, this approach failed to meet the required accuracy of few % for two main reasons as follows.

- (i) The majority of the β decays are measured using β - γ coincidences, which are sensitive to the so-called pandemonium effect [26]. The net result is an experimental bias of the shape of the energy spectra, with the high energy part being overestimated relative to the low energy part. New measurements are ongoing with dedicated experimental setups to correct for the pandemonium effect, but in the case of the reference spectra many unstable nuclei have to be studied.
- (ii) As mentioned above, an important fraction of the detected neutrinos has a large energy (>4 MeV). The associated β transitions mostly come from very unstable nuclei with a large energy gap between the parent ground state and the nuclear levels of the daughter nucleus. Their decay scheme is often poorly known or even not measured at all.

A reference data set was constituted based on all fission products indexed in the ENSDF database [27]. All nuclei measured separately to correct for the pandemonium effect were substituted when not in agreement with the ENSDF data (67 nuclei from [28] and 29 nuclei from [29]). A dedicated interface, BESTIOLE, reads the relevant information of this set of almost 10000 β -branches and computes their energy spectrum based on (4). Then, the total beta spectrum of one fissioning isotope is built as the sum of all fission fragment spectra is weighted by their activity. These activities are determined using a simulation package called MCNP Utility for Reactor Evolution (MURE [30]). Following this procedure, the predicted fission spectrum is about 90% of the reference ILL β spectra, as illustrated in Figure 2 for the ^{235}U isotope. The missing contribution is the image of all unmeasured decays as well as the remaining experimental biases of the measurements. To fill the gap one can invoke models of the decay scheme of missing fission products. Reaching a good agreement with the ILL electron data remains difficult with this approach.

Another way to fill the gap is to fit the missing contribution in the electron spectrum with few virtual branches. The same ILL procedure can be used except that the virtual branches now rest on the base of physical transitions. This mixed approach combines the assets of *ab initio* and virtual branches methods as follows.

- (i) The prediction still matches accurately the reference electron data from the ILL measurements.
- (ii) 90% of the spectrum is built with measured β transitions with “true” distributions of endpoint, branching ratios, nuclear charges, and so forth. This suppresses the impact of the approximations associated with the use of virtual beta branches.
- (iii) All corrections to the Fermi theory are applied at the branch level, preserving the correspondence between the reference electron data and the predicted antineutrino spectrum.

The new predicted antineutrino spectra are found about 3% above the ILL spectra. This effect is comparable for the 3 isotopes (^{235}U , ^{239}Pu , and ^{241}Pu) with little energy

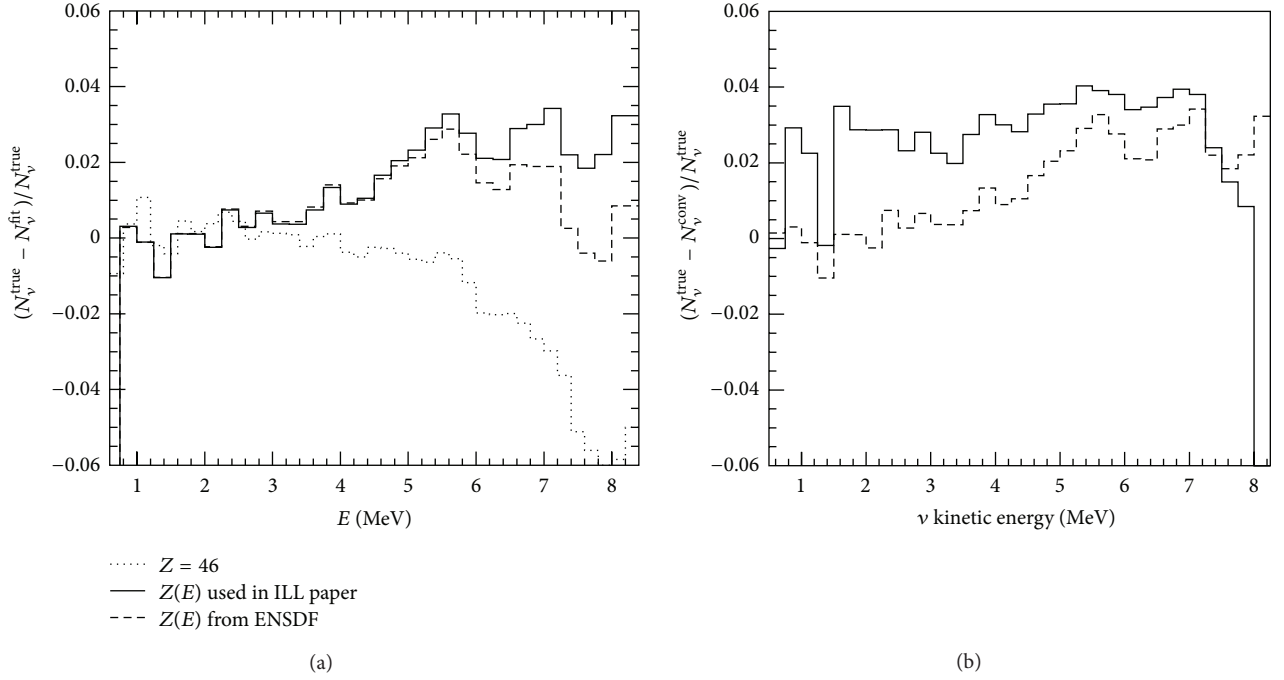


FIGURE 1: Numerical tests of the conversion-induced deviations from a “true” spectrum built from a set of known branches (see text for details). (a) Effect of various $Z(E)$ polynomials used in the formula of the virtual branches. (b) Deviation of converted spectra with the effective correction of (6) (solid line) or with the correction applied at the branch level.

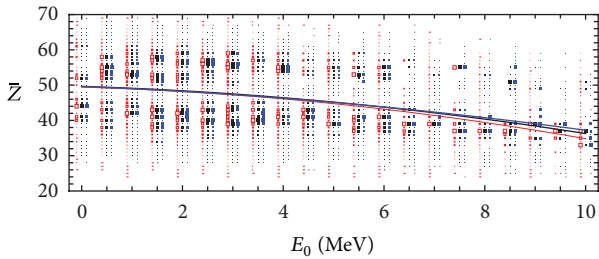


FIGURE 2: The effective nuclear charge \bar{Z} of the fission fragments of ^{235}U as a function of E_0 . The area of the each box is proportional to the contribution of that particular Z to the fission yield in that energy bin. The lines are fits of quadratic polynomials. Black color-ENSDF database; other colors illustrate the small sensitivity to different treatment of the missing isotopes.

dependence. The origin and the amplitude of this bias could be numerically studied in detail following a method initially developed in [31]. A “true” electron spectrum is defined as the sum of all measured branches. Since all the branches are known, the “true” antineutrino spectrum is perfectly defined as well, with no uncertainty from the conversion. Applying the exact same conversion procedure than in the eighties on this new electron reference confirms the 3% shift between the converted antineutrino spectrum and the “true” spectrum.

Further tests have shown that this global 3% shift is actually a combination of two effects. At high energy ($E > 4$ MeV), the proper distribution of nuclear charges, provided by the dominant contribution of the physical β -branches,

induces a 3% increase of the predicted antineutrino spectrum. On the low energy side, it was shown that the effective linear correction of (6) was not accounting for the cancellations operating between the numerous physical branches when the correction is applied at the branch level (see Figure 1).

Beyond the correction of these above biases, the uncertainty of the new fission antineutrino spectra couldn’t be reduced with respect to the initial predictions. The normalisation of the ILL electron data, a dominant source of error, is inherent to any conversion procedure using the electron reference. Then, a drawback of the extensive use of measured β -branches in the mixed approach is that it brings important constraints on the missing contribution to reach the electron data. In particular, the induced missing shape can be difficult to fit with virtual branches, preventing a perfect match with the electron reference. These electron residuals are unfortunately amplified as spurious oscillations in the predicted antineutrino spectrum leading to comparable conversion uncertainties (see red curve in Figure 3). Finally, the correction of the weak magnetism effect is calculated in a quite crude way, and the same approximations are used since the eighties.

In the light of the above results, the initial conversion procedure of the ILL data was revisited [32]. It was shown that a fit using only virtual branches with a judicious choice of the effective nuclear charge could provide results with minimum bias. A mean fit similar to (5) is still used, but the nuclear charge of all known branches is now weighted by its contribution in the total spectrum, that is, the associated fission yield. As shown in Figure 2, the result is quite stable under various assumptions for the weighting of poorly known

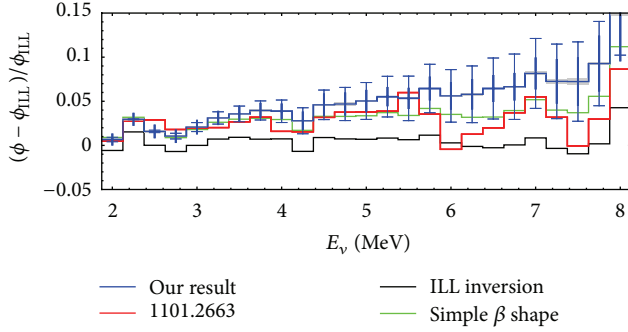


FIGURE 3: Comparison of different conversions of the ILL electron data for ^{235}U . Black curve: cross-check of results from [19] following the same procedure. Red curve: results from [22]. Green curve: results from [32] using the same description of β decay as in [22]. Blue curve: update of the results from [22], including corrections to the Fermi theory as explained in the text. The thin error bars show the theory errors from the effective nuclear charge \bar{Z} and weak magnetism. The thick error bars are the statistical errors.

nuclei. The bias illustrated in the left plot of Figure 1 is corrected.

The second bias (Figure 1(b)) is again corrected by implementing the corrections to the Fermi theory at the branch level rather than using effective corrections as in (6). Using the same expression of these corrections than in [22], the two independent new predictions are in very good agreement (Figure 3), confirming the 3% global shift. Note that the spurious oscillations of the Mueller et al. spectra are flattened out by this new conversion because of the better zeroing of electron residuals.

A detailed review of all corrections to the Fermi theory is provided in [32] including finite size corrections, screening correction, radiative corrections, and weak magnetism. To a good approximation, they all appear as linear correction terms as illustrated in Figure 4 in the case of a 10 MeV endpoint energy. This refined study of all corrections leads to an extra increase of the predicted antineutrino spectra at high energy as illustrated by the blue curve in Figure 3. The net effect is between 1.0% and 1.4% more detected antineutrinos depending on the isotope (see Table 1).

The corrections of Figure 4 are known with a good relative accuracy except for the weak magnetism term. At the present time, a universal slope factor of about 0.5% per MeV is assumed, neglecting any dependence on nuclear structure [25]. Accurate calculation for every fission product is out of reach. Using the conserved vector current hypothesis, it is possible to infer the weak magnetism correction from the electromagnetic decay of isobaric analog states. Examples of the slope factors computed from the available data are shown in Table I of [32]. While most examples are in reasonable agreement with the above universal slope, some nuclei with large value of $\log ft$ have a very large slope factor. Moreover, a review of the nuclear databases [33] shows that β transitions with $\log ft > 7$ contribute between 15 and 30% to the total spectrum. Still the data on the weak magnetism slopes are scarce, and none of them corresponds to fission products. At

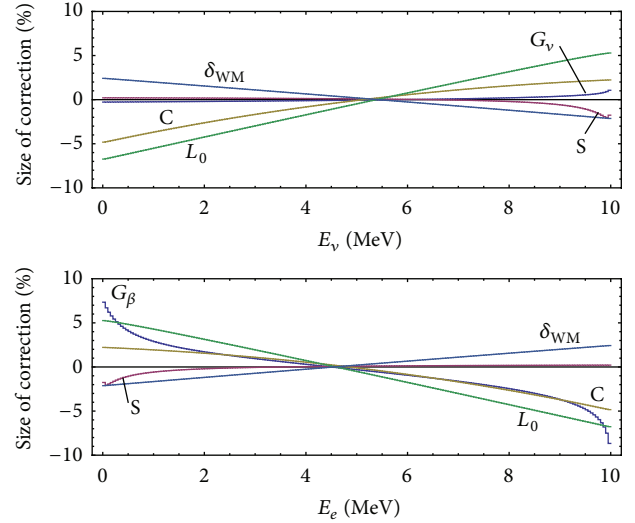


FIGURE 4: Shown is the relative size of the various corrections to the Fermi theory for a hypothetical β decay with $Z = 46$, $A = 117$, and $E_0 = 10$ MeV. The upper panel shows the effect on the antineutrino spectrum, whereas the lower panel shows the effect on the β spectrum. δ_{WM} : weak magnetism correction; L_0 , C: Coulomb and weak interaction finite size corrections; S screening correction; $G_{\nu,\beta}$: radiative corrections.

TABLE 1: Relative change of the new predicted events rates with respect to the ILL reference (in %). The relative change of the emitted flux is always close to 3%, dominated by the few first bins because the energy spectra are dropping fast.

$(R_{\text{new}} - R_{\text{ILL}})/R_{\text{ILL}}$	^{235}U	^{239}Pu	^{241}Pu	^{238}U
Values from [22]	2.5	3.1	3.7	9.8
Values from [32]	3.7	4.2	4.7	—

this stage, it is difficult to conclude if the uncertainty of the weak magnetism correction should be inflated or not. The prescription of the ILL analysis, 100%, corresponds to about 1% of the detected neutrino rate. The best constraints could actually come from shape analysis of the reactor neutrino data themselves. The Bugey and Rovno data are accurate although detailed information on the detector response might be missing for such a detailed shape analysis. The combination of the upcoming Daya Bay, Double Chooz, and RENO data should soon set stringent limits on the global slope factor.

The error budget of the predicted spectra remains again comparable to the first ILL analysis. The normalization error of the electron data is a common contribution. The uncertainties of the conversion by virtual branches have been extensively studied and quantified based on the numerical approach. The uncertainty induced by the weak magnetism corrections is, *faute de mieux*, evaluated with the same 100% relative error. The final central values and errors are summarized in table [22].

2.3. Off-Equilibrium Effects. For an accurate analysis of reactor antineutrino data, an extra correction to the reference fission spectra has to be applied. It is often of the order of

the percent. It comes from the fact that the ILL spectra were acquired after a relatively short irradiation time, between 12 hours and 1.8 days depending on the isotopes, whereas in a reactor experiment the typical time scale is several months. A nonnegligible fraction of the fission products have a lifetime of several days. Therefore, the antineutrinos associated with their β decay keep accumulating well after the “photograph at 1 day” of the spectra taken at ILL. Very long-lived isotopes correspond to nuclei close to the bottom of the nuclear valley of stability. Hence, one naively expects these β transitions to contribute at low energy. For a quantitative estimate of this effect, the same simulations developed in [22] for the *ab initio* calculation of antineutrino spectra were used. The sensitivity to the nuclear ingredients is suppressed because only the relative changes between the ILL spectra and spectra of longer irradiations at commercial reactors were computed. The corrections to be applied are summarized in [22]. As expected, they concern the low energy part of the detected spectrum and vanish beyond 3.5 MeV. The corrections are larger for the ^{235}U spectrum because its irradiation time, 12 h, is shorter than the others. The uncertainty was estimated from the comparison between the results of MURE and FISPAC codes as well as from the sensitivity to the simulated core geometry. A safe 30% relative error is recommended.

2.4. ^{238}U Reference Spectrum. The ^{238}U isotope is contributing to about 8% of the total number of fissions in a standard commercial reactor. These fissions are induced by fast neutrons therefore, their associated β -spectrum could not be measured in the purely thermal flux of ILL. A dedicated measurement in the fast neutron flux of the FRMII reactor in Munich has been completed and should be published in the coming months [34].

Meanwhile the *ab initio* calculation developed in [22] provides a useful prediction since the relatively small contribution of ^{238}U can accommodate larger uncertainties in the predicted antineutrino spectrum. An optimal set of β -branches was tuned to match the ILL spectra of fissile isotopes as well as possible. The base of this data set consists of the ENSDF branches corrected for the pandemonium effect as described in Section 2.2. Missing β emitters are taken from the JENDL nuclear database [35], where they are calculated using the gross-theory [36]. Finally, the few remaining nuclei were described using a model based on fits of the distributions of the endpoints and branching ratios in the ENSDF database, then extrapolated to the exotic nuclei.

The comparison with the reference ^{235}U ILL data shows that the predicted spectrum agrees with the reference at the $\pm 10\%$ level.

Then, this optimal data set is used to predict a ^{238}U spectrum. Again the activity of each fission product is calculated with the evolution code MURE. The case of an N4 commercial reactor operating for one year was simulated. After such a long irradiation time, the antineutrino spectrum has reached the equilibrium. The results are summarized in [22]. The central values are about 10% higher than the previous prediction proposed in [37]. This discrepancy might be due to the larger amount of nuclei taken into account in the

most recent work. Nevertheless, both results are comparable within the uncertainty of the prediction, roughly estimated from the deviation with respect to the ILL data and the sensitivity to the chosen data set.

2.5. Summary of the New Reactor Antineutrino Flux Prediction. In summary, a reevaluation of the reference antineutrino spectra associated to the fission of ^{235}U , ^{239}Pu , and ^{241}Pu isotopes [22] has revealed some systematic biases in the previously published conversion of the ILL electron data [19–21]. The net result is a $\approx +3\%$ shift in the predicted emitted spectra. The origin of these biases was not in the principle of the conversion method but in the approximate treatment of nuclear data and corrections to the Fermi theory. A complementary work [32] confirmed the origin of the biases and showed that an extra correction term should be added increasing further the predicted antineutrino spectra at high energy. These most recent spectra are the new reference used for the analysis of the reactor anomaly in the next section. The prediction of the last isotope contributing to the neutrino flux of reactors, ^{238}U , is also updated by *ab initio* calculations.

The new predicted spectra and their errors are presented in [22]. The deviations with respect to the old reference spectra are given in Table 1.

3. Investigating Neutrino Oscillations

3.1. Exploring the Solar Oscillation. The sun is a well-defined neutrino source to provide important opportunities of investigating nontrivial neutrino properties because of the wide range of matter density and the great distance from the sun to the earth. Precise measurement of solar neutrinos is a direct test of the standard solar model (SSM) that is developed from the stellar structure and evolution.

Solar neutrinos have been observed by several experiments: Homestake with a chlorine detector, SAGE, GALLEX and GNO with gallium detectors, Kamiokande and Super-Kamiokande with water Cherenkov detectors, and SNO with a heavy water detector. Most recently, Borexino has successfully observed low energy solar neutrinos with their energy spectrum using a liquid scintillator detector of ultra low radioactivity.

The first observation of solar neutrinos by the Homestake experiment demonstrated the significantly smaller measured flux than the SSM prediction, known as “the solar neutrino puzzle” at that time. SAGE, GALLEX, and GNO are sensitive to the most abundant *pp* solar neutrinos, and also observed the deficit. Kamiokande-II and Super-Kamiokande succeeded in real-time and directional measurement of solar neutrinos in a water Cherenkov detector. The solar neutrino problem was solved by SNO through the flavor-dependent measurement using heavy water. In 2001, the initial SNO charged current result combined with the Super-Kamiokande’s high-statistics νe elastic scattering result provided direct evidence for flavor conversion of solar neutrinos. The later SNO neutral current measurements further strengthened the conclusion. These results are consistent with those expected from the large mixing angle (LMA) solution of

solar neutrino oscillation in matter with $\Delta m_{\text{sol}}^2 \sim 5 \times 10^{-5} \text{ eV}^2$ and $\tan^2 \theta_{\text{sol}} \sim 0.45$.

The KamLAND reactor neutrino experiment at a flux-weighted average distance of $\sim 180 \text{ km}$ obtained a result of reactor antineutrino disappearance consistent with the LMA solar neutrino solution. The current solar neutrino and KamLAND data suggest that $\Delta m_{21}^2 = (7.50 \pm 0.20) \times 10^{-5} \text{ eV}^2$ with a fractional error of 2.7% and $\sin^2 2\theta_{12} = 0.857 \pm 0.024$ with a fractional error of 2.8%.

3.2. Exploring the Atmospheric Oscillation. The Super-Kamiokande obtained the first convincing evidence for the neutrino oscillation in the observation of the atmospheric neutrinos, in 1998. A clear deficit of atmospheric muon neutrino candidate events was observed in the zenith-angle distribution compared to the no-oscillation expectation. The distance-to-energy L/E distribution of the Super-Kamiokande data demonstrated $\nu_\mu \leftrightarrow \nu_\tau$ oscillations and completely ruled out some of exotic explanations of the atmospheric neutrino disappearance such as neutrino decay and quantum decoherence.

Accelerator experiments can better measure the value of $|\Delta m_{\text{atm}}^2|$ than the atmospheric neutrino observation due to a fixed baseline distance and a well-understood neutrino spectrum. K2K is the first long-baseline experiment to study ν_μ oscillations in the atmospheric Δm^2 region with a neutrino path length exceeding hundreds of kilometers. MINOS is the second long-baseline experiment for the atmospheric neutrino oscillation using a ν_μ beam. The MINOS finds the atmospheric oscillation parameters as $|\Delta m_{\text{atm}}^2| = (2.32_{-0.08}^{+0.12}) \times 10^{-3} \text{ eV}^2$ and $\sin^2 2\theta_{\text{atm}} > 0.90$ at 90% C.L. OPERA using the CNGS ν_μ beam reported observation of one ν_τ candidate. T2K began a new long-baseline experiment in 2010, and is expected to measure $|\Delta m_{\text{atm}}^2|$ and $\sin^2 \theta_{\text{atm}}$ even more precisely. Nova is expected to be in operation soon for the accurate measurement of atmospheric neutrino oscillation parameters.

The current atmospheric neutrino and accelerator data suggest that $\Delta m_{32(31)}^2 = (2.32_{-0.08}^{+0.12}) \times 10^{-3} \text{ eV}^2$ with a fractional error of 4.3% and $\sin^2 2\theta_{23} = 0.97 \pm 0.03$ with a fractional error of 3.1%.

3.3. Measuring the Last and Smallest Neutrino Mixing Angle θ_{13} . In the presently accepted paradigm to describe the neutrino oscillations, there are three mixing angles (θ_{12} , θ_{23} , and θ_{13}) and one phase angle (δ) in the Pontecorvo-Maki-Nakagawa-Sakata matrix [38–40]. It was until 2012 that θ_{13} is the most poorly known and smallest mixing angle.

Measurements of θ_{13} are possible using reactor neutrinos and accelerator neutrino beams. Reactor measurements have the property of determining θ_{13} without the ambiguities associated matter effects and CP violation. In addition, the detector for a reactor measurement is not necessarily large, and the construction of a neutrino beam is not needed. The past reactor measurement had a single detector which was placed about 1 km from the reactors. The new generation reactor experiments, Daya Bay, Double Chooz, and RENO, using two detectors of 10 ~ 40 tons at near (300 ~ 400 m)

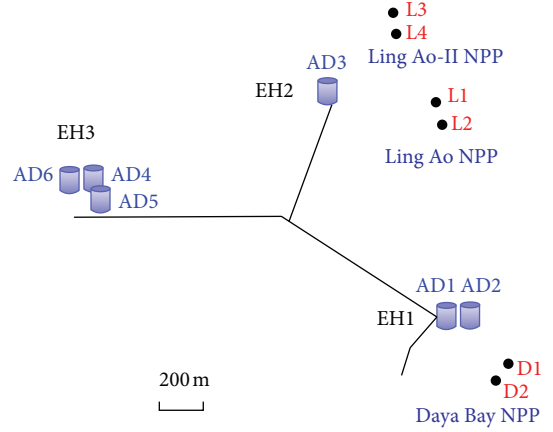


FIGURE 5: Layout of the Daya Bay experiment. The dots represent reactors, labeled as D1, D2, L1, L2, L3 and L4. Six ADs, AD1–AD6, are installed in three EHs.

and far (1 ~ 2 km) locations have significantly improved sensitivity for θ_{13} down to the $\sin^2(2\theta_{13}) \sim 0.01$ level. With θ_{13} determined and measurements of $\nu_\mu \rightarrow \nu_e$ and $\bar{\nu}_\mu \rightarrow \bar{\nu}_e$ oscillations using accelerator neutrino beams impinging on large detectors at long baselines will improve the knowledge of θ_{13} and also allow access to matter or CP violation effects.

Previous attempts at measuring θ_{13} via neutrino oscillations have obtained only upper limits [41–43]; the CHOOZ [41, 42] and MINOS [44] experiments set the most stringent limits: $\sin^2 2\theta_{13} < 0.15$ (90% C.L.). In 2011, indications of a nonzero θ_{13} value were reported by two accelerator appearance experiments, T2K [45] and MINOS [46], and by the Double Chooz reactor disappearance experiment [47, 48]. Global analyses of all available neutrino oscillation data have indicated central values of $\sin^2 2\theta_{13}$ that are between 0.05 and 0.1 (see e.g., [49, 50]). In 2012, Daya Bay and RENO reported definitive measurements of the neutrino oscillation mixing angle, θ_{13} , based on the disappearance of electron antineutrinos emitted from reactors. The θ_{13} measurements by the three reactor experiments are presented in the following sections.

4. Daya Bay

The Daya Bay collaboration announced on March 8, 2012, the discovery of a nonzero value for the last unknown neutrino mixing angle θ_{13} [51], based on 55 days of data taking. It is consistent with previous and subsequent measurements [45–48, 52]. An improved analysis using 139 days of data is reported at international conferences, and a paper is now under preparation [53].

4.1. The Experiment. The Daya Bay nuclear power complex is located on the Southern coast of China, 55 km to the northeast of Hong Kong and 45 km to the East of Shenzhen. A detailed description of the Daya Bay experiment can be found in [54]. As shown in Figure 5, the nuclear complex consists of six pressurized water reactors grouped into three pairs with each pair referred to as a nuclear power plant (NPP). All six

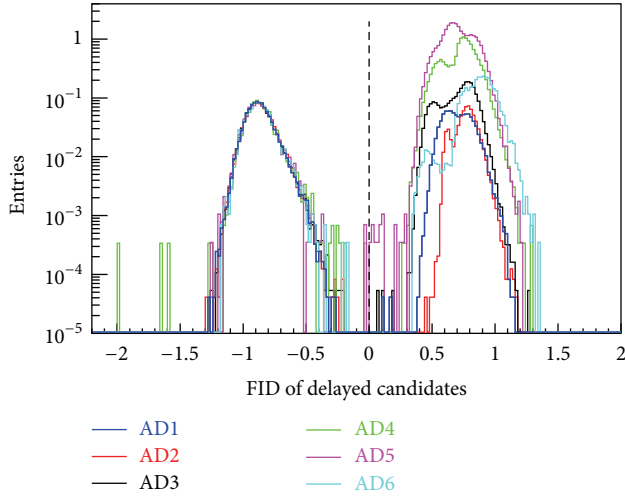


FIGURE 7: Discrimination of flasher events and IBD-delayed signals in the neutron energy region. The delayed signals of IBDs have the same distribution for all six ADs, while the flashers are different.

4.2. Data, Monte Carlo Simulation, and Event Reconstruction. The data used in this analysis were collected from December 24, 2011 through May 11, 2012.

The detector halls operated independently, linked only by a common clock and GPS timing system. As such, data from each hall were recorded separately and linked offline. Simultaneous operation of all three detector halls is required to minimize systematic effects associated with potential reactor power excursions.

Triggers were formed based either on the number of PMTs with signals above a ~ 0.25 photoelectron (pe) threshold (Nhit triggers) or the charge sum of the over-threshold PMTs (E-Sum trigger).

A small number of AD PMTs, called flashers, spontaneously emit light, presumably due to a discharge within the base. The visible energy of such events covers a wide range, from sub-MeV to 100 MeV. Two features were typically observed when a PMT flashed. The observed charge for a given PMT was very high with light seen by the surrounding PMTs, and PMTs on the opposite side of the AD saw light from the flasher.

To reject flasher events, a flasher identification variable (FID) was constructed. Figure 7 shows the discrimination of flasher events for the delayed signal of IBD candidates. The inefficiency for selection was estimated to be 0.02%. The uncorrelated uncertainties among ADs were estimated to be 0.01%. The contamination of the IBD selection was evaluated to be $< 10^{-4}$.

The AD energy response has a time dependence, a detector spatial dependence (nonuniformity), and a particle species and energy dependence (nonlinearity). The goal of energy reconstruction was to correct these dependences in order to minimize the AD energy scale uncertainty. The LEDs were utilized for PMT gain calibration, while the energy scale was determined with a ^{60}Co source deployed at the detector center. The sources were deployed once per week to check for and correct any time dependence.

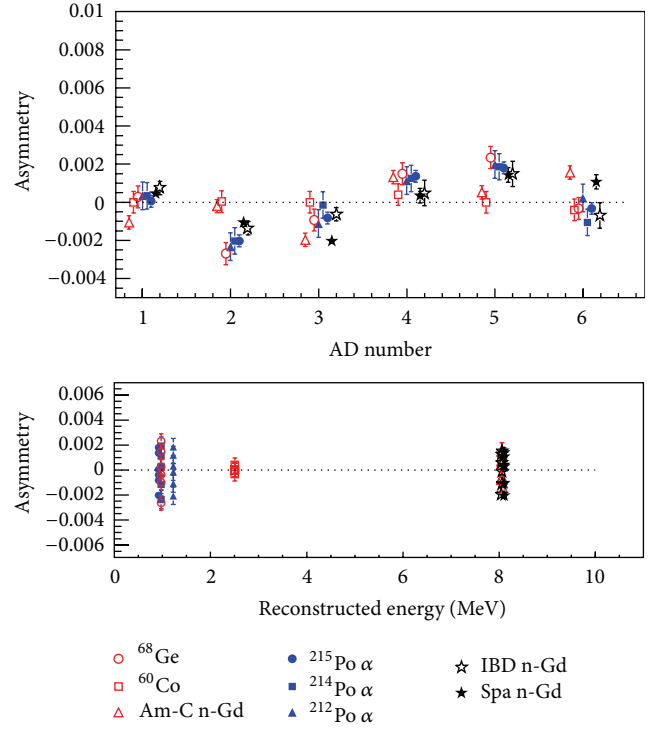


FIGURE 8: Asymmetry values for all six ADs. The sources ^{68}Ge , ^{60}Co , and Am-C were deployed at the detector center. The alphas from polonium decay and neutron capture on gadolinium from IBD and spallation neutrons were uniformly distributed within each detector. Differences between these sources are due to spatial nonuniformity of detector response.

A scan along the z -axis utilizing the ^{60}Co source from each of the three ACUs was used to obtain nonuniformity correction functions. The nonuniformity was also studied with spallation neutrons generated by cosmic muons and alphas produced by natural radioactivity present in the liquid scintillator. The neutron energy scale was set by comparing ^{60}Co events with neutron capture on Gd events from the Am-C source at the detector center. Additional details of energy calibration and reconstruction can be found in [54]. Asymmetries in the mean of the six ADs' response are shown in Figure 8. Asymmetries for all types of events in all the ADs fall within a narrow band, and the uncertainty is estimated to be 0.5%, uncorrelated among ADs.

A Geant4 [60] based computer simulation (Monte Carlo, MC) of the detectors and readout electronics was used to study detector response and consisted of five components: kinematic generator, detector simulation, electronics simulation, trigger simulation, and readout simulation. The MC is carefully tuned, by taking measured parameters of the materials properties, to match observed detector distributions, such as PMT timing, charge response, and energy nonlinearity. An optical model is developed to take into account photon absorption and reemission processes in liquid scintillator.

4.3. Event Selection, Efficiencies, and Uncertainties. Two preselections were completed prior to IBD selection. First, flasher

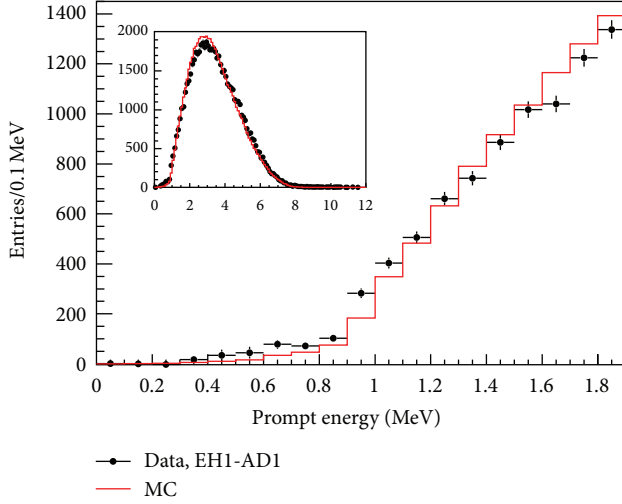


FIGURE 9: The prompt energy spectrum from AD1. IBD selection required $0.7 < E_p < 12.0$ MeV. Accidental backgrounds were subtracted, where the spectrum of accidental background was estimated from the spectrum of all >0.7 MeV triggers.

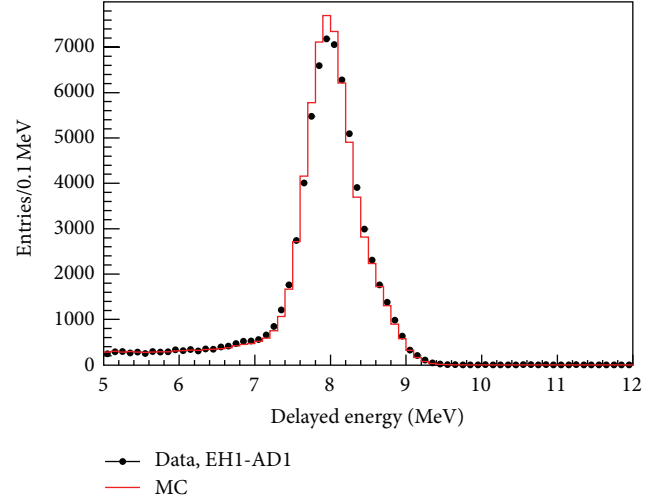


FIGURE 10: The delayed energy spectrum from AD1. IBD selection required $6.0 < E_d < 12.0$ MeV. Accidental backgrounds were subtracted, where the spectrum of accidental background was estimated from the spectrum of single neutrons.

events were rejected. Second, triggers within a $(-2\mu\text{s}, 200\mu\text{s})$ window with respect to a water shield muon candidate (μ_{WS}) were rejected, where a μ_{WS} was defined as any trigger with $N_{\text{hit}} > 12$ in either the inner or outer water shield. This allowed for the removal of most of the false triggers that followed a muon, as well as triggers associated with the decay of spallation products. Events in an AD within $\pm 2\mu\text{s}$ of a μ_{WS} with energy > 20 MeV or > 2.5 GeV were classified as AD muons (μ_{AD}) or showering muons (μ_{sh}), respectively.

Within an AD, only prompt-delayed pairs separated in time by less than $200\mu\text{s}$ ($1 < t_d - t_p < 200\mu\text{s}$, where t_p and t_d are time of the prompt and delayed signal, resp.) with no intervening triggers and no $E > 0.7$ MeV triggers within $200\mu\text{s}$ before the prompt signal or $200\mu\text{s}$ after the delayed signal were selected (referred to as the multiplicity cut). A prompt-delayed pair was vetoed if the delayed signal is in coincidence with a water shield muon ($-2\mu\text{s} < t_d - t_{\mu_{\text{WS}}} < 600\mu\text{s}$) or an AD muon ($0 < t_d - t_{\mu_{\text{AD}}} < 1000\mu\text{s}$) or a showering muon ($0 < t_d - t_{\mu_{\text{sh}}} < 1$ s). The energy of the delayed candidate must be $6.0\text{ MeV} < E_d < 12.0\text{ MeV}$, while the energy of the prompt candidate must be $0.7\text{ MeV} < E_p < 12.0\text{ MeV}$. The prompt energy, the delayed energy and the capture time distributions for data and MC are shown in Figures 9, 10, and 11, respectively.

The data are generally in good agreement with the MC. The apparent difference between data and MC in the prompt energy spectrum is due to nonlinearity of the detector response; however, the correction to this nonlinearity was not performed in this analysis. Since all ADs had similar nonlinearity (as shown in the bottom panel of Figure 8), and the energy selection cuts cover a larger range than the actual distribution, the discrepancies introduced negligible uncertainties to the rate analysis.

For a relative measurement, the absolute efficiencies and correlated uncertainties do not factor into the error

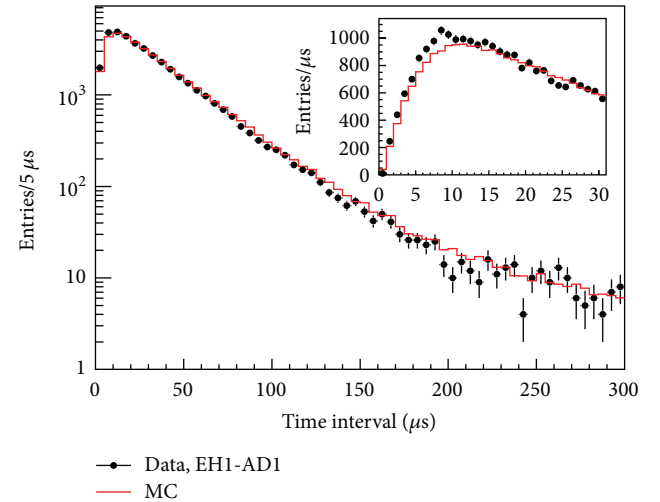


FIGURE 11: The neutron capture time from AD1. IBD selection required $1 < t_d - t_p < 200\mu\text{s}$. In order to compare data with MC, a cut on prompt energy ($E_p > 3$ MeV) was applied to reject accidental backgrounds.

budget. In that regard, only the uncorrelated uncertainties matter. Extracting absolute efficiencies and correlated errors were done in part to better understand our detector, and it was a natural consequence of evaluating the uncorrelated uncertainties. Efficiencies associated with the prompt energy, delayed energy, capture time, Gd capture fraction, and spill-in effects were evaluated with the Monte Carlo. Efficiencies associated with the muon veto, multiplicity cut, and livetime were evaluated using data. In general, the uncorrelated uncertainties were not dependent on the details of our computer simulation.

Table 3 is a summary of the absolute efficiencies and the systematic uncertainties. The uncertainties of the absolute

TABLE 3: Summary of absolute efficiencies and systematic uncertainties. For our relative measurement, only the uncorrelated uncertainties contribute to the final error in our relative measurement.

	Efficiency	Correlated	Uncorrelated
Target protons		0.47%	0.03%
Flasher cut	99.98%	0.01%	0.01%
Delayed energy cut	90.9%	0.6%	0.12%
Prompt energy cut	99.88%	0.10%	0.01%
Multiplicity cut		0.02%	<0.01%
Capture time cut	98.6%	0.12%	0.01%
Gd capture ratio	83.8%	0.8%	<0.1%
Spill-in	105.0%	1.5%	0.02%
Livetime	100.0%	0.002%	<0.01%

efficiencies were correlated among the ADs. No relative efficiency, except $\epsilon_{\mu}\epsilon_m$, was corrected. All differences between the functionally identical ADs were taken as uncorrelated uncertainties. Detailed description of the analysis can be found in [53].

4.4. Backgrounds. Backgrounds are actually the main source of systematic uncertainties of this experiment; even though the background to signal ratio is only a few percent. Extensive studies show that cosmic-ray-induced backgrounds are the main component, while AmC neutron sources installed at the top of our neutrino detector for calibration contribute also to a significant portion. Although the random coincidence background is the largest, its uncertainty is well under control. Table 4 lists all the signal and background rates as well as their uncertainties. A detailed study can be found in [53].

The accidental background was defined as any pair of otherwise uncorrelated triggers that happen to satisfy the IBD selection criteria. They can be easily calculated based on textbooks, and their uncertainties are well understood. When calculating the rate of accidental backgrounds listed in Table 4, A correction is needed to account for the muon veto efficiency and the multiplicity cut efficiency. An alternate method, called the off-windows method, was developed to determine accidental backgrounds. This result was also validated by comparing the prompt-delayed distance of accidental coincidences selected by the off-windows method with IBD candidates. The relative differences between off-windows method results and theoretical calculation of 6 ADs were less than 1%.

Energetic neutrons entering an AD aped IBD by recoiling off a proton before being captured on Gd. The number of fast neutron background events in the IBD sample is estimated by extrapolating the prompt energy (E_p) distribution between 12 and 100 MeV down to 0.7 MeV. Two different extrapolation methods were used; one is a flat distribution, and the other one is a first-order polynomial function. The fast neutron background in the IBD sample was assigned to be equal to the mean value of the two extrapolation methods, and the systematic error was determined from the sum of their differences and the fitting uncertainties. As a check, the fast

neutrons prompt energy spectrum associated with tagged muons validates our extrapolation method.

The rate of correlated background from the β - n cascade of ${}^9\text{Li}$ / ${}^8\text{He}$ decays was evaluated from the distribution of the time since the last muon and can be described by a sum of exponential functions with different time constant [61]. To reduce the number of minimum ionizing muons in these data samples, we assumed that most of the ${}^9\text{Li}$ and ${}^8\text{He}$ production was accompanied with neutron generation. The muon samples with and without reduction were both prepared for ${}^9\text{Li}$ and ${}^8\text{He}$ background estimation. By considering binning effects and differences between results with and without muon reduction, we assigned a 50% systematical error to the final result.

The ${}^{13}\text{C}(\alpha n){}^{16}\text{O}$ background was determined by measuring alpha decay rates in situ and then by using MC to calculate the neutron yield. We identified four sources of alpha decays, the ${}^{238}\text{U}$, ${}^{232}\text{Th}$, ${}^{227}\text{Ac}$ decay chains, and ${}^{210}\text{Po}$ taking into account half lives of their decay chain products, 164.3 μs , 0.3 μs , and 1.781 ms, respectively. Geant4 was used to model the energy deposition process. Based on JENDL [62] (αn) cross-sections, the neutron yield as a function of energy was calculated and summed. Finally, with the in-situ measured alpha decay rates and the MC determined neutron yields, the ${}^{13}\text{C}(\alpha n){}^{16}\text{O}$ rate was calculated.

During data taking, the Am-C sources sat inside the ACUs on top of each AD. Neutrons emitted from these sources would occasionally ape IBD events by scattering inelastically with nuclei in the shielding material (emitting gamma rays) before being captured on a metal nuclei, such as Fe, Cr, Mn, or Ni (releasing more gamma rays). We estimated the neutron-like events from the Am-C sources by subtracting the number of neutron-like singles in the $Z < 0$ region from the $Z > 0$ region. The Am-C correlated background rate was estimated by MC simulation normalized using the Am-C neutron-like event rate obtained from data. Even though the agreement between data and MC is excellent for Am-C neutron-like events, we assigned 100% uncertainty to the estimated background due to the Am-C sources to account for any potential uncertainty in the neutron capture cross-sections used by the simulation.

4.5. Side-By-Side Comparison in EH1. Relative uncertainties were studied with data by comparing side-by-side antineutrino detectors. A detailed comparison using three months of data from ADs in EH1 has been presented elsewhere [54]. An updated comparison of the prompt energy spectra of IBD events for the ADs in EH1 using 231 days of data (Sep. 23, 2011 to May 11, 2012) is shown in Figure 12 after correcting for efficiencies and subtracting background. A bin-by-bin ratio of the AD1 and AD2 spectra is also shown. The ratio of total IBD rates in AD1 and AD2 was measured to be 0.987 ± 0.004 (stat.) ± 0.003 (syst.), consistent with the expected ratio of 0.982. The difference in rates was primarily due to differences in baselines of the two ADs in addition to a slight dependence on the individual reactor on/off status. It was known that AD2 has a 0.3% lower energy response than AD1 for uniformly distributed events, resulting in a slight tilt

TABLE 4: Signal and background summary. The background and IBD rates were corrected for the $\epsilon_\mu \epsilon_m$ efficiency.

	AD1	AD2	AD3	AD4	AD5	AD6
IBD candidates	69121	69714	66473	9788	9669	9452
Expected IBDs	68613	69595	66402	9922.9	9940.2	9837.7
DAQ livetime (days)	127.5470		127.3763		126.2646	
Muon veto time (days)	22.5656	22.9901	18.1426	2.3619	2.3638	2.4040
$\epsilon_\mu \epsilon_m$	0.8015	0.7986	0.8364	0.9555	0.9552	0.9547
Accidentals (per day)	9.73 ± 0.10	9.61 ± 0.10	7.55 ± 0.08	3.05 ± 0.04	3.04 ± 0.04	2.93 ± 0.03
Fast neutron (per day)	0.77 ± 0.24	0.77 ± 0.24	0.58 ± 0.33	0.05 ± 0.02	0.05 ± 0.02	0.05 ± 0.02
$^9\text{Li}/^8\text{He}$ (per AD per day)	2.9 ± 1.5		2.0 ± 1.1		0.22 ± 0.12	
Am-C correlated (per AD per day)	0.2 ± 0.2					
$^{13}\text{C}(\alpha n)^{16}\text{O}$ background (per day)	0.08 ± 0.04	0.07 ± 0.04	0.05 ± 0.03	0.04 ± 0.02	0.04 ± 0.02	0.04 ± 0.02
IBD rate (per day)	662.47 ± 3.00	670.87 ± 3.01	613.53 ± 2.69	77.57 ± 0.85	76.62 ± 0.85	74.97 ± 0.84

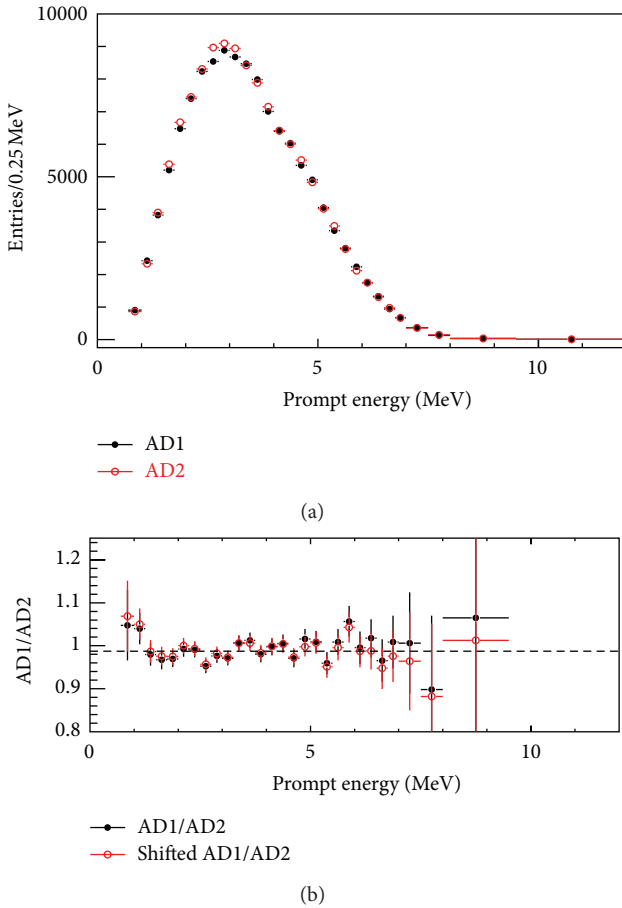


FIGURE 12: The energy spectra for the prompt signal of IBD events in AD1 and AD2 (a) are shown along with the bin-by-bin ratio (b). Within (b), the dashed line represents the ratio of the total rates for the two ADs, and the open circles show the ratio with the AD2 energy scaled by +0.3%.

to the distribution shown in Figure 12(b). The distribution of open circles was created by scaling the AD2 energy by 0.3%. The distribution with scaled AD2 energy agrees well with a flat distribution.

4.6. Reactor Neutrino Flux. Reactor antineutrinos result primarily from the beta decay of the fission products of four main isotopes, ^{235}U , ^{239}Pu , ^{238}U , and ^{241}Pu . The $\bar{\nu}_e$ flux of each reactor ($S(E)$) was predicted from the simulated fission fraction f_i and the neutrino spectra per fission (S_i) [19–22, 32, 37] of each isotope [63],

$$S(E) = \frac{W_{\text{th}}}{\sum_k f_k E_k} \sum_i f_i S_i(E), \quad (7)$$

where i and k sum over the four isotopes, E_i is the energy released per fission, and W_{th} is the measured thermal power.

The thermal power data were provided by the power plant. The uncertainties were dominated by the flow rate measurements of feedwater through three parallel cooling loops in each core [63–65]. The correlations between the flow meters were not clearly known. We conservatively assume that they were correlated for a given core but were uncorrelated between cores, giving a maximal uncertainty for the experiment. The assigned uncorrelated uncertainty for thermal power was 0.5%.

A simulation of the reactor cores using commercial software (SCIENCE [66, 67]) provided the fission fraction as a function of burnup. The fission fraction carries a 5% uncertainty set by the validation of the simulation software. The 3D spatial distribution of the isotopes within a core was also provided by the power plant, although simulation indicated that it had a negligible effect on acceptance. A complementary core simulation package was developed based on DRAGON [68] as a cross-check and for systematic studies. The code was validated with the Takahama-3 benchmark [69] and agreed with the fission fraction provided by the power plant to 3%. Correlations among the four isotopes were studied using the DRAGON-based simulation package, and agreed well with the data collected in [70]. Given the constraints of the thermal power and correlations, the uncertainties of the fission fraction simulation translated into a 0.6% uncorrelated uncertainty in the neutrino flux.

The neutrino spectrum per fission is a correlated uncertainty that cancels out for a relative measurement. The reaction cross-section for isotope i was defined as $\sigma_i = \int S_i(E_\nu) \sigma(E_\nu) dE_\nu$, where $S_i(E_\nu)$ is the neutrino spectra per

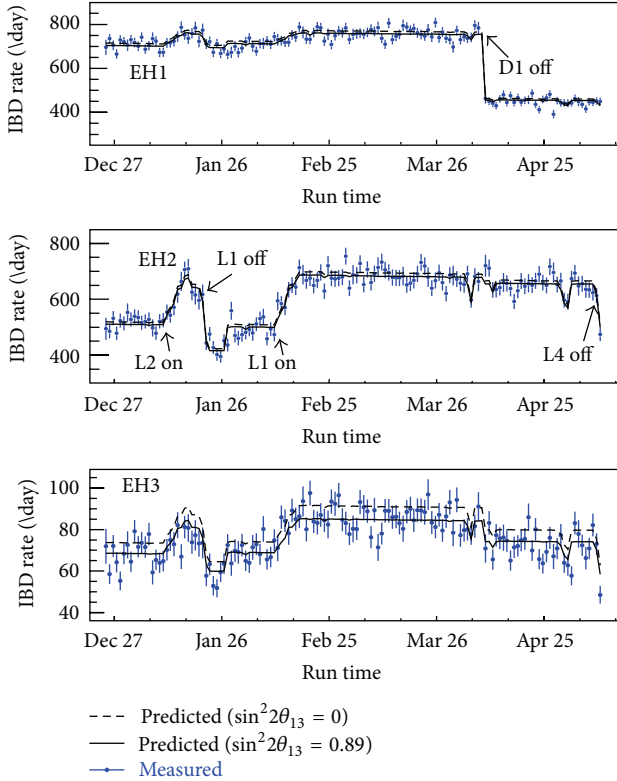


FIGURE 13: The daily average measured IBD rates per AD in the three experimental halls are shown as a function of time along with predictions based on reactor flux analyses and detector simulation.

fission and $\sigma(E_\mu)$ is the IBD cross-section. We took the reaction cross-section from [10] but substituted the IBD cross-section with that in [71]. The energy released per fission and its uncertainties were taken from [72]. Nonequilibrium corrections for long-lived isotopes were applied following [22]. Contributions from spent fuel [73, 74] ($\sim 0.3\%$) were included as an uncertainty.

The uncertainties in the baseline and the spatial distribution of the fission fractions in the core had a negligible effect to the results.

Figure 13 presents the background-subtracted and efficiency-corrected IBD rates in the three experimental halls. Predicted IBD rate from reactor flux calculation and detector Monte Carlo simulation are shown for comparison. The dashed lines have been corrected with the best-fit normalization parameter ε in (10) to get rid of the biases from the absolute reactor flux uncertainty and the absolute detector efficiency uncertainty.

4.7. Results. The $\bar{\nu}_e$ rate in the far hall was predicted with a weighted combination of the two near hall measurements assuming no oscillation. A ratio of measured-to-expected rate is defined as

$$R = \frac{M_f}{\bar{N}_f} = \frac{M_f}{\alpha M_a + \beta M_b}, \quad (8)$$

TABLE 5: Reactor-related uncertainties.

Correlated		Uncorrelated	
Energy/fission	0.2%	Power	0.5%
IBD reaction/fission	3%	Fission fraction	0.6%
		Spent fuel	0.3%
Combined	3%	Combined	0.8%

where \bar{N}_f and M_f are the predicted and measured rates in the far hall (sum of AD 4–6) and M_a and M_b are the measured IBD rates in EH1 (sum of AD 1–2) and EH2 (AD3), respectively. The values for α and β were dominated by the baselines and only slightly dependent on the integrated flux of each core. For the analyzed data set, $\alpha = 0.0439$ and $\beta = 0.2961$. The residual reactor-related uncertainty in R was 5% of the uncorrelated uncertainty of a single core. The deficit observed at the far hall was as follows:

$$R = 0.944 \pm 0.007 \text{ (stat)} \pm 0.003 \text{ (syst)}. \quad (9)$$

The value of $\sin^2 2\theta_{13}$ was determined with a χ^2 constructed with pull terms accounting for the correlation of the systematic errors [75] as follows:

$$\chi^2 = \sum_{d=1}^6 \frac{[M_d - T_d(1 + \varepsilon + \sum_r \omega_r^d \alpha_r + \varepsilon_d) + \eta_d]^2}{M_d + B_d} + \sum_r \frac{\alpha_r^2}{\sigma_r^2} + \sum_{d=1}^6 \left(\frac{\varepsilon_d^2}{\sigma_d^2} + \frac{\eta_d^2}{\sigma_B^2} \right), \quad (10)$$

where M_d is the measured IBD events of the d th AD with backgrounds subtracted, B_d is the corresponding background, T_d is the prediction from neutrino flux, MC, and neutrino oscillations, and ω_r^d is the fraction of IBD contribution of the r th reactor to the d th AD determined by baselines and reactor fluxes. The uncorrelated reactor uncertainty is σ_r (0.8%), as shown in Table 5. σ_d (0.2%) is the uncorrelated detection uncertainty, listed in Table 8. σ_B is the background uncertainty listed in Table 4. The corresponding pull parameters are $(\alpha_r, \varepsilon_d, \text{ and } \eta_d)$. The detector- and reactor-related correlated uncertainties were not included in the analysis; the absolute normalization ε was determined from the fit to the data.

The survival probability used in the χ^2 was

$$P_{\text{sur}} = 1 - \sin^2 2\theta_{13} \sin^2 \left(1.267 \Delta m_{31}^2 \frac{L}{E} \right) - \cos^4 \theta_{13} \sin^2 2\theta_{12} \sin^2 \left(1.267 \Delta m_{21}^2 \frac{L}{E} \right), \quad (11)$$

where $\Delta m_{31}^2 = 2.32 \times 10^{-3} \text{ eV}^2$, $\sin^2 2\theta_{12} = 0.861^{+0.026}_{-0.022}$, and $\Delta m_{21}^2 = 7.59^{+0.20}_{-0.21} \times 10^{-5} \text{ eV}^2$. The uncertainty in Δm_{31}^2 had negligible effect and thus was not included in the fit.

The best-fit value is

$$\sin^2 2\theta_{13} = 0.089 \pm 0.010 \text{ (stat.)} \pm 0.005 \text{ (syst.)} \quad (12)$$

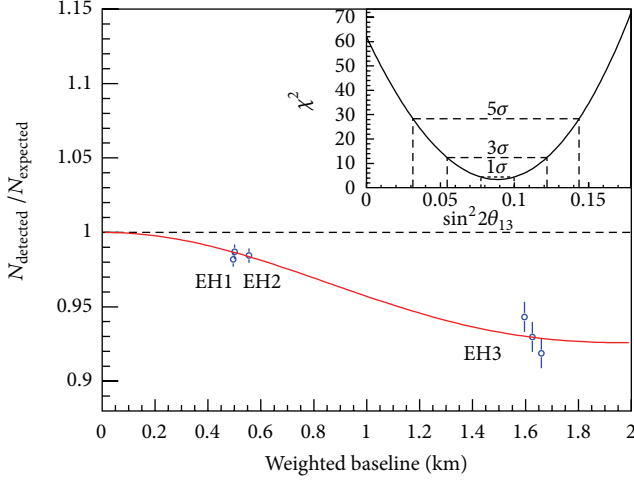


FIGURE 14: Ratio of measured versus expected signal in each detector, assuming no oscillation. The error bar is the uncorrelated uncertainty of each AD. The expected signal was corrected with the best-fit normalization parameter. The oscillation survival probability at the best-fit value is given by the smooth curve. The AD4 and AD6 data points were displaced by -30 and $+30$ m for visual clarity. The χ^2 versus $\sin^2 2\theta_{13}$ is shown in the inset.

with a χ^2/NDF of 3.4/4. All best estimates of pull parameters are within its one standard deviation based on the corresponding systematic uncertainties. The no-oscillation hypothesis is excluded at 7.7 standard deviations. Figure 14 shows the measured number of events in each detector, relative to those expected assuming no oscillation. A $\sim 1.5\%$ oscillation effect appears in the near halls. The oscillation survival probability at the best-fit values is given by the smooth curve. The χ^2 versus $\sin^2 2\theta_{13}$ is shown in the inset.

The observed $\bar{\nu}_e$ spectrum in the far hall was compared to a prediction based on the near hall measurements $\alpha M_a + \beta M_b$ in Figure 15. The distortion of the spectra is consistent with the expected one calculated with the best-fit θ_{13} obtained from the rate-only analysis, providing further evidence of neutrino oscillation.

5. Double Chooz

The Double Chooz detector system (Figure 16) consists of a main detector, an outer veto, and calibration devices. The main detector comprises four concentric cylindrical tanks filled with liquid scintillators or mineral oil. The innermost 8 mm thick transparent (UV to visible) acrylic vessel houses the 10 m^3 ν -target liquid, a mixture of n-dodecane, PXE, PPO, bis-MSB, and 1 g gadolinium/l as a beta-diketonate complex. The scintillator choice emphasizes radiopurity and long-term stability. The ν -target volume is surrounded by the γ -catcher, a 55 cm thick Gd-free liquid scintillator layer in a second 12 mm thick acrylic vessel, used to detect γ -rays escaping from the ν -target. The light yield of the γ -catcher was chosen to provide identical photoelectron (pe) yield across these two layers. Outside the γ -catcher is the buffer, a 105 cm

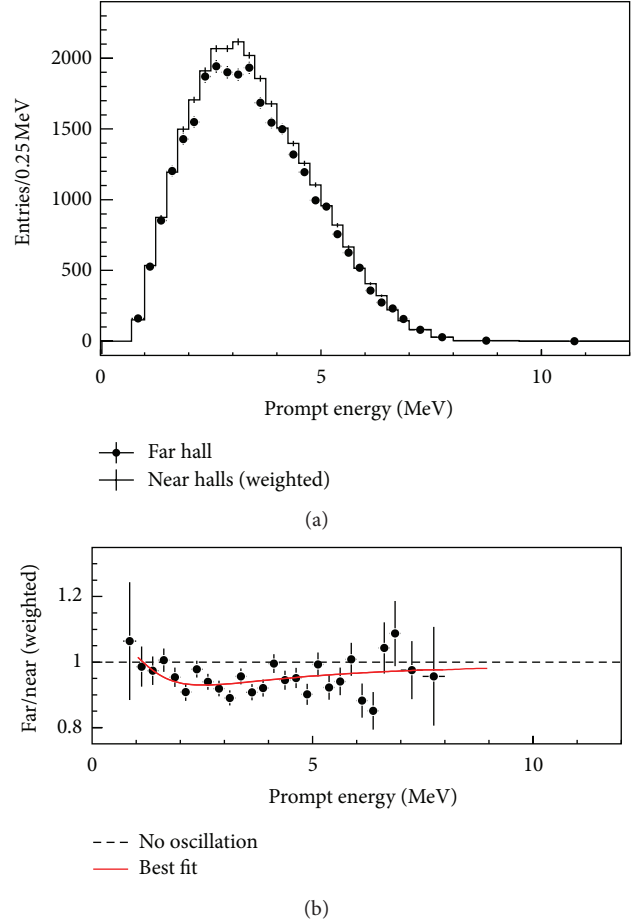


FIGURE 15: (a) Measured prompt energy spectrum of the far hall (sum of three ADs) compared with the no-oscillation prediction from the measurements of the two near halls. Spectra were background subtracted. Uncertainties are statistical only. (b) The ratio of measured and predicted no-oscillation spectra. The red curve is the best-fit solution with $\sin^2 2\theta_{13} = 0.089$ obtained from the rate-only analysis. The dashed line is the no-oscillation prediction.

thick mineral oil layer. The buffer works as a shield to γ -rays from radioactivity of PMTs and from the surrounding rock and is one of the major improvements over the CHOOZ detector. It shields from radioactivity of photomultipliers (PMTs) and of the surrounding rock, and it is one of the major improvements over the CHOOZ experiment. 390 10-inch PMTs are installed on the stainless steel buffer tank inner wall to collect light from the inner volumes. These three volumes and the PMTs constitute the inner detector (ID). Outside the ID, and optically separated from it, is a 50 cm thick inner veto liquid scintillator (IV). It is equipped with 78 8-inch PMTs and functions as a cosmic muon veto and as a shield to spallation neutrons produced outside the detector. The detector is surrounded by 15 cm of demagnetized steel to suppress external γ -rays. The main detector is covered by an outer veto system. The readout is triggered by custom energy sum electronics. The ID PMTs are separated into two groups of 195 PMTs uniformly distributed throughout the volume, and the PMT signals in each group are summed.

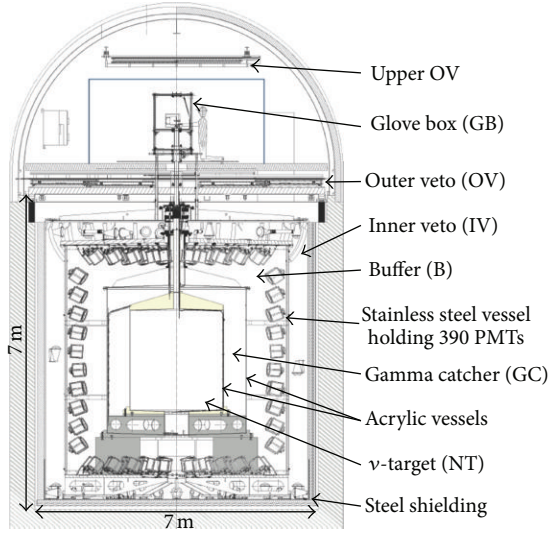


FIGURE 16: A cross-sectional view of the Double Chooz detector system.

The signals of the IV PMTs are also summed. If any of the three sums is above a set energy threshold, the detector is read out with 500 MHz flash-ADC electronics with customized firmware and a dead time-free acquisition system. Upon each trigger, a 256 ns interval of the waveforms of both ID and IV signals is recorded. Having reduced the ambient radioactivity enables us to set a low trigger rate (120 Hz) allowed the ID readout threshold to be set at 350 keV, well below the 1.02 MeV minimum energy of an IBD positron, greatly reducing the threshold systematics. The experiment is calibrated by several methods. A multiwavelength LED-fiber light injection system (LI) produces fast light pulses illuminating the PMTs from fixed positions. Radio-isotopes ^{137}Cs , ^{68}Ge , ^{60}Co , and ^{252}Cf were deployed in the target along the vertical symmetry axis and, in the gamma catcher, through a rigid loop traversing the interior and passing along boundaries with the target and the buffer. The detector was monitored using spallation neutron captures on H and Gd, residual natural radioactivity, and daily LI runs. The energy response was found to be stable within 1% over time.

5.1. Chooz Reactor Modeling. Double Chooz's sources of antineutrinos are the reactor cores B1 and B2 at the Électricité de France (EDF) Centrale Nucléaire de Chooz, two N4 type pressurized water reactor (PWR) cores with nominal thermal power outputs of 4.25 GW_{th} each. The instantaneous thermal power of each reactor core P_{th}^R is provided by EDF as a fraction of the total power. It is derived from the in-core instrumentation with the most important variable being the temperature of the water in the primary loop. The dominant uncertainty on the weekly heat balance at the secondary loops comes from the measurement of the water flow. At the nominal full power of 4250 MW, the final uncertainty is 0.5% (1 σ C.L.). Since the amount of data taken with one or two cores at intermediate power is small, this uncertainty is used for the mean power of both cores.

The antineutrino spectrum for each fission isotope is taken from [22, 32], including corrections for off-equilibrium effects. The uncertainty on these spectra is energy dependent but is on the order of 3%. The fractional fission rates α_k of each isotope are needed in order to calculate the mean cross-section per fission. They are also required for the calculation of the mean energy released per fission for reactor R:

$$\langle E_f \rangle_R = \sum_k \alpha_k \langle E_f \rangle_k. \quad (13)$$

The thermal power one would calculate given a fission is relatively insensitive to the specific fuel composition since the $\langle E_f \rangle_k$ differ by <6%; however, the difference in the detected number of antineutrinos is amplified by the dependence of the norm and mean energy of $S_k(E)$ on the fissioning isotope. For this reason, much effort has been expended in developing simulations of the reactor cores to accurately model the evolution of the α_k .

Double Chooz has chosen two complementary codes for modeling of the reactor cores: MURE and DRAGON [30, 76–78]. These two codes provide the needed flexibility to extract fission rates and their uncertainties. These codes were benchmarked against data from the Takahama-3 reactor [79]. The construction of the reactor model requires detailed information on the geometry and materials comprising the core. The Chooz cores are comprised of 205 fuel assemblies. For every reactor fuel cycle, approximately one year in duration, one-third of the assemblies are replaced with assemblies containing fresh fuel. The other two-thirds of the assemblies are redistributed to obtain a homogeneous neutron flux across the core. The Chooz reactor cores contain four assembly types that differ mainly in their initial ^{235}U enrichment. These enrichments are 1.8%, 3.4%, and 4%. The data set reported here spans fuel cycle 12 for core B2 and cycle 12 and the beginning of cycle 13 for B1. EDF provides Double Chooz with the locations and initial burnup of each assembly. Based on these maps, a full core simulation was constructed using MURE for each cycle. The uncertainty due to the simulation technique is evaluated by comparing the DRAGON and MURE results for the reference simulation leading to a small 0.2% systematic uncertainty in the fission rate fractions α_k . Once the initial fuel composition of the assemblies is known, MURE is used to model the evolution of the full core in time steps of 6 to 48 hours. This allows the α_k 's, and therefore the predicted antineutrino flux, to be calculated. The systematic uncertainties on the α_k 's are determined by varying the inputs and observing their effect on the fission rate relative to the nominal simulation. The uncertainties considered are those due to the thermal power, boron concentration, moderator temperature and density, initial burnup error, control rod positions, choice of nuclear databases, choice of the energies released per fission, and statistical error of the MURE Monte Carlo. The two largest uncertainties come from the moderator density and control rod positions.

In far-only phase of Double Chooz, the rather large uncertainties in the reference spectra limit the sensitivity to

TABLE 6: The uncertainties in the antineutrino prediction. All uncertainties are assumed to be correlated between the two reactor cores. They are assumed to be normalization and energy (rate and shape) unless noted as normalization only.

Source	Normalization only	Uncertainty (%)
P_{th}	Yes	0.5
$\langle\sigma_f\rangle^{\text{Bugey}}$	Yes	1.4
$S_k(E)\sigma_{\text{IBD}}(E_{\nu}^{\text{true}})$	No	0.2
$\langle E_f \rangle$	No	0.2
L_R	Yes	<0.1
α_k^R	No	0.9
Total		1.8

θ_{13} . To mitigate this effect, the normalization of the cross-section per fission for each reactor is anchored to the Bugey-4 rate measurement at 15 m [10]:

$$\langle\sigma_f\rangle_R = \langle\sigma_f\rangle^{\text{Bugey}} + \sum_k (\alpha_k^R - \alpha_k^{\text{Bugey}}) \langle\sigma_f\rangle_k, \quad (14)$$

where R stands for each reactor. The second term corrects the difference in fuel composition between Bugey-4 and each of the Chooz cores. This treatment takes advantage of the high accuracy of the Bugey-4 anchor point (1.4%) and suppresses the dependence on the predicted $\langle\sigma_f\rangle_R$. At the same time, the analysis becomes insensitive to possible oscillations at shorter baselines due to heavy $\Delta m^2 \sim 1 \text{ eV}^2$ sterile neutrinos. The expected number of antineutrinos with no oscillation in the i th energy bin with the Bugey-4 anchor point becomes as follows:

$$N_i^{\text{exp},R} = \frac{\epsilon N_p}{4\pi} \frac{1}{L_R^2} \frac{P_{\text{th}}^R}{\langle E_f \rangle_R} \times \left(\frac{\langle\sigma_f\rangle_R}{\left(\sum_k \alpha_k^R \langle\sigma_f\rangle_k\right)} \sum_k \alpha_k^R \langle\sigma_f\rangle_k^i \right), \quad (15)$$

where ϵ is the detection efficiency, N_p is the number of protons in the target, L_R is the distance to the center of each reactor, and P_{th}^R is the thermal power. The variable $\langle E_f \rangle_R$ is the mean energy released per fission defined in (13), while $\langle\sigma_f\rangle_R$ is the mean cross-section per fission defined in (14). The three variables P_{th}^R , $\langle E_f \rangle_R$, and $\langle\sigma_f\rangle_R$ are time dependent with $\langle E_f \rangle_R$ and $\langle\sigma_f\rangle_R$ depending on the evolution of the fuel composition in the reactor and P_{th}^R depending on the operation of the reactor. A covariance matrix $M_{ij}^{\text{exp}} = \delta N_i^{\text{exp}} \delta N_j^{\text{exp}}$ is constructed using the uncertainties listed in Table 6.

The IBD cross-section used is the simplified form from Vogel and Beacom [71]. The cross-section is inversely proportional to the neutron lifetime. The MAMBO-II measurement of the neutron lifetime [80] is being used, leading to $K = 0.961 \times 10^{-43} \text{ cm}^2 \text{ MeV}^{-2}$.

5.2. Modeling the Double Chooz Detector. The detector response uses a detailed Geant4 [81, 82] simulation with enhancements to the scintillation process, photocathode

optical surface model, and thermal neutron model. Simulated IBD events are generated with run-by-run correspondence of MC to data, with fluxes and rates calculated as described in the previous paragraph. Radioactive decays in calibration sources and spallation products were simulated using detailed models of nuclear levels, taking into account branching ratios and correct spectra for transitions [83–85]. Optical parameters used in the detector model are based on detailed measurements made by the collaboration. Tuning of the absolute and relative light yield in the simulation was done with calibration data. The scintillator emission spectrum was measured using a Cary Eclipse Fluorometer [86]. The photon emission time probabilities used in the simulation are obtained with a dedicated laboratory setup [87]. For the ionization quenching treatment in our MC, the light output of the scintillators after excitation by electrons [88] and alpha particles [89] of different energies was measured. The nonlinearity in light production in the simulation has been adjusted to match these data. The finetuning of the total attenuation was made using measurements of the complete scintillators [87]. Other measured optical properties include reflectivities of various detector surfaces and indices of refraction of detector materials.

The readout system simulation (RoSS) accounts for the response of elements associated with detector readout, such as from the PMTs, FEE, FADCs, trigger system and DAQ. The simulation relies on the measured probability distribution function (PDF) to empirically characterize the response to each single PE as measured by the full readout channel. The Geant4-based simulation calculates the time at which each PE strikes the photocathode of each PMT. RoSS converts this time per PE into an equivalent waveform as digitized by FADCs. After calibration, the MC and data energies agree within 1%.

A set of Monte Carlo $\bar{\nu}_e$ events representing the expected signal for the duration of physics data taking is created based on the formalism of (16). The calculated IBD rate is used to determine the rate of interactions. Parent fuel nuclide and neutrino energies are sampled from the calculated neutrino production ratios and corresponding spectra, yielding a properly normalized set of IBD-progenitor neutrinos. Once generated, each event-progenitor neutrino is assigned a random creation point within the originating reactor core. The event is assigned a weighted random interaction point within the detector based on proton density maps of the detector materials. In the center-of-mass frame of the ν - p interaction, a random positron direction is chosen, with the positron and neutron of the IBD event given appropriate momenta based on the neutrino energy and decay kinematics. These kinematic values are then boosted into the laboratory frame. The resulting positron and neutron momenta and originating vertex are then available as inputs to the Geant4 detector simulation. Truth information regarding the neutrino origin, baseline, and energy are propagated along with the event, for use later in the oscillation analysis.

5.3. Event Reconstruction. The pulse reconstruction provides the signal charge and time in each PMT. The baseline mean (B_{mean}) and rms (B_{rms}) are computed using the full readout

window (256 ns). The integrated charge (q) is defined as the sum of digital counts in each waveform sample over the integration window, once the pedestal has been subtracted. For each pulse reconstructed, the start time is computed as the time when the pulse reaches 20% of its maximum. This time is then corrected by the PMT-to-PMT offsets obtained with the light injection system.

Vertex reconstruction in Double Chooz is not used for event selection but is used for event energy reconstruction. It is based on a maximum charge and time likelihood algorithm which utilizes all hit and no-hit information in the detector. The performance of the reconstruction has been evaluated in situ using radioactive sources deployed at known positions along the z -axis in the target volume, and off-axis in the guide tubes. The sources are reconstructed with a spatial resolution of 32 cm for ^{137}Cs , 24 cm for ^{60}Co , and 22 cm for ^{68}Ge .

Cosmic muons passing through the detector or the nearby rock induce backgrounds which are discussed later. The IV trigger rate is 46 s^{-1} . All muons in the ID are tagged by the IV except some stopping muons which enter the chimney. Muons which stop in the ID and their resulting Michel e can be identified by demanding a large energy deposition (roughly a few tens of MeV) in the ID. An event is tagged as a muon if there is $>5 \text{ MeV}$ in the IV or $>30 \text{ MeV}$ in the ID.

The visible energy (E_{vis}) provides the absolute calorimetric estimation of the energy deposited per trigger. E_{vis} is a function of the calibrated PE (total number of photoelectrons):

$$E_{\text{vis}} = PE^m(\rho, z, t) \times f_u^m(\rho, z) \times f_s^m(t) \times f_{\text{MeV}}^m, \quad (16)$$

where $PE = \sum_i pe_i = \sum_i q_i / \text{gain}_i(q_i)$. Coordinates in the detector are ρ and z , t is time, m refers to data or Monte Carlo (MC), and i refers to each good channel. The correction factors f_u , f_s , and f_{MeV} correspond, respectively, to the spatial uniformity, time stability, and photoelectron per MeV calibrations. Four stages of calibration are carried out to render E_{vis} linear, independent of time and position, and consistent between data and MC. Both the MC and data are subjected to the same stages of calibration. The sum over all good channels of the reconstructed raw charge (q_i) from the digitized waveforms is the basis of the energy estimation. The PE response is position dependent for both MC and data. Calibration maps were created such that any PE response for any event located at any position (ρ, z) can be converted into its response as if measured at the center of the detector ($\rho = 0, z = 0$): $PE_{\odot}^m = PE^m(\rho, z) \times f_u^m(\rho, z)$. The calibration map's correction for each point is labeled $f_u^m(\rho, z)$. Independent uniformity calibration maps $f_u^m(\rho, z)$ are created for data and MC, such that the uniformity calibration serves to minimize any possible difference in position dependence of the data with respect to MC. The capture peak on H (2.223 MeV) of neutrons from spallation and antineutrino interactions provides a precise and copious calibration source to characterize the response nonuniformity over the full volume (both NT and GC).

The detector response stability was found to vary in time due to two effects, which are accounted for and corrected by the term $f_s^m(t)$. First, the detector response can change due to

TABLE 7: Energy scale systematic errors.

	Error (%)
Relative nonuniformity	0.43
Relative instability	0.61
Relative nonlinearity	0.85
Total	1.13

variations in readout gain or scintillator response. This effect has been measured as a +2.2% monotonic increase over 1 year using the response of the spallation neutrons capturing on Gd within the NT. Second, few readout channels varying over time are excluded from the calorimetry sum, and the average overall response decreases by 0.3% per channel excluded. Therefore, any response $PE_{\odot}(t)$ is converted to the equivalent response at t_0 , as $PE_{\odot}^m(t_0) = PE_{\odot}^m(t) \times f_s^m(t)$. The t_0 was defined as the day of the first Cf source deployment, during August 2011. The remaining instability after calibration is used for the stability systematic uncertainty estimation.

The number PE_{\odot}^m per MeV is determined by an absolute energy calibration independently, for the data and MC. The response in PE_{\odot}^m for H capture as deployed in the center of the NT is used for the absolute energy scale. The absolute energy scales are found to be $229.9 PE_{\odot}^m / \text{MeV}$ and $227.7 PE_{\odot}^m / \text{MeV}$, respectively, for the data and MC, demonstrating agreement within 1% prior to this calibration stage.

Discrepancies in response between the MC and data, after calibration, are used to estimate these uncertainties within the prompt energy range and the NT volume. Table 7 summarizes the systematic uncertainty in terms of the remaining nonuniformity, instability, and nonlinearity. The relative nonuniformity systematic uncertainty was estimated from the calibration maps using neutrons capturing on Gd, after full calibration. The rms deviation of the relative difference between the data and MC calibration maps is used as the estimator of the nonuniformity systematic uncertainty, and is 0.43%. The relative instability systematic error, discussed above, is 0.61%. A 0.85% variation consistent with this nonlinearity was measured with the z -axis calibration system, and this is used as the systematic error for relative nonlinearity in Table 7. Consistent results were obtained when sampling with the same sources along the GT.

5.4. Neutrino Data Analysis. Signals and Backgrounds. The $\bar{\nu}_e$ candidate selection is as follows. Events with an energy below 0.5 MeV, where the trigger efficiency is not 100%, or identified as light noise ($Q_{\text{max}}/Q_{\text{tot}} > 0.09$ or $\text{rms}(t_{\text{start}}) > 40 \text{ ns}$), are discarded. Triggers within a 1 ms window following a tagged muon are also rejected in order to reduce the correlated and cosmogenic backgrounds. The effective veto time is 4.4% of the total run time. Defining $\Delta T \equiv t_{\text{delayed}} - t_{\text{prompt}}$, further selection consists of 4 cuts:

- (1) time difference between consecutive triggers (prompt and delayed): $2 \mu\text{s} < \Delta T < 100 \mu\text{s}$, where the lower cut reduces correlated backgrounds and the upper cut

TABLE 8: Cuts used in the event selection and their efficiency for IBD events. The OV was working for the last 68.9% of the data.

Cut	Efficiency %
E_{prompt}	100.0 \pm 0.0
E_{delayed}	94.1 \pm 0.6
ΔT	96.2 \pm 0.5
Multiplicity	99.5 \pm 0.0
Muon veto	90.8 \pm 0.0
Outer veto	99.9 \pm 0.0

is determined by the approximately 30 μs capture time on Gd;

- (2) prompt trigger: $0.7 \text{ MeV} < E_{\text{prompt}} < 12.2 \text{ MeV}$;
- (3) delayed trigger: $6.0 \text{ MeV} < E_{\text{delayed}} < 12.0 \text{ MeV}$ and $Q_{\text{max}}/Q_{\text{tot}} < 0.055$;
- (4) multiplicity: no additional triggers from 100 μs preceding the prompt signal to 400 μs after it, with the goal of reducing the correlated background.

The IBD efficiencies for these cuts are listed in Table 8.

A preliminary sample of 9021 candidates is obtained by applying selections (1–4). In order to reduce the background contamination in the sample, candidates are rejected according to two extra cuts. First, candidates within a 0.5 s window after a high energy muon crossing the ID ($E_{\mu} > 600 \text{ MeV}$) are tagged as cosmogenic isotope events and are rejected, increasing the effective veto time to 9.2%. Second, candidates whose prompt signal is coincident with an OV trigger are also excluded as correlated background. Applying the above vetoes yields 8249 candidates or a rate of 36.2 ± 0.4 events/day, uniformly distributed within the target, for an analysis livetime of 227.93 days. Following the same selection procedure on the $\bar{\nu}_e$ MC sample yields 8439.6 expected events in the absence of oscillation.

The main source of accidental coincidences is the random association of a prompt trigger from natural radioactivity and a later neutron-like candidate. This background is estimated not only by applying the neutrino selection cuts described, but also using coincidence windows shifted by 1 s in order to remove correlations in the time scale of n-captures in H and Gd. The radioactivity rate between 0.7 and 12.2 MeV is 8.2 s^{-1} , while the singles rate in 6–12 MeV energy region is 18 h^{-1} . Finally, the accidental background rate is found to be 0.261 ± 0.002 events per day.

The radioisotopes ^8He and ^9Li are products of spallation processes on ^{12}C induced by cosmic muons crossing the scintillator volume. The β -n decays of these isotopes constitute a background for the antineutrino search. β -n emitters can be identified from the time and space correlations to their parent muon. Due to their relatively long lifetimes (^9Li : $\tau = 257 \text{ ms}$, ^8He : $\tau = 172 \text{ ms}$), an event-by-event discrimination is not possible. For the muon rates in our detector, vetoing for several isotope lifetimes after each muon would lead to an unacceptably large loss in exposure. Instead, the rate is determined by an exponential fit to the $\Delta t_{\mu\nu} \equiv t_{\mu} - t_{\nu}$ profile of all possible muon-IBD candidate pairs. The

analysis is performed for three visible energy E_{μ}^{vis} ranges that characterize subsamples of parent muons by their energy deposition, not corrected for energy nonlinearities, in the ID as follows.

- (1) Showering muons crossing the target value are selected by $E_{\mu}^{\text{vis}} > 600 \text{ MeV}$, and feature, they an increased probability to produce cosmogenic isotopes. The $\Delta t_{\mu\nu}$ fit returns a precise result of 0.95 ± 0.11 events/day for the β -n-emitter rate.
- (2) In the E_{μ}^{vis} range from 275 to 600 MeV, muons crossing GC and target still give a sizable contribution to isotope production of 1.08 ± 0.44 events/day. To obtain this result from a $\Delta t_{\mu\nu}$ fit, the sample of muon-IBD pairs has to be cleaned by a spatial cut on the distance of closest approach from the muon to the IBD candidate of $d_{\mu\nu} < 80 \text{ cm}$ to remove the majority of uncorrelated pairs. The corresponding cut efficiency is determined from the lateral distance profile obtained for $E_{\mu}^{\text{vis}} > 600 \text{ MeV}$. The approach is validated by a comparative study of cosmic neutrons that show an almost congruent profile with very little dependence on E_{μ}^{vis} above 275 MeV.
- (3) The cut $E_{\mu}^{\text{vis}} < 275 \text{ MeV}$ selects muons crossing only the buffer volume or the rim of the GC. For this sample, no production of β -n emitters inside the target volume is observed. An upper limit of < 0.3 events/day can be established based on a $\Delta t_{\mu\nu}$ fit for $d_{\mu\nu} < 80 \text{ cm}$. Again, the lateral distribution of cosmic neutrons has been used for determining the cut efficiency.

The overall rate of βn decays found is $2.05^{+0.62}_{-0.52}$ events/day.

Most correlated backgrounds are rejected by the 1 ms veto time after each tagged muon. The remaining events arise from cosmogenic events whose parent muon either misses the detector or deposits an energy low enough to escape the muon tagging. Two contributions have been found: fast neutrons (FNs) and stopping muons (SMs). FNs are created by muons in the inactive regions surrounding the detector. Their large interaction length allows them to cross the detector and capture in the ID, causing both a prompt trigger by recoil protons and a delayed trigger by capture on Gd. An approximately flat prompt energy spectrum is expected; a slope could be introduced by acceptance and scintillator quenching effects. The time and spatial correlations distribution of FN are indistinguishable from those of $\bar{\nu}_e$ events. The selected SM arise from muons entering through the chimney, stopping in the top of the ID, and eventually decaying. The short muon track mimics the prompt event, and the decay Michel electron mimics the delayed event. SM candidates are localized in space in the top of the ID under the chimney and have a prompt-delayed time distribution following the 2.2 μs muon lifetime. The correlated background has been studied by extending the selection on E_{prompt} up to 30 MeV. No IBD events are expected in the interval $12 \text{ MeV} \leq E_{\text{prompt}} \leq 30 \text{ MeV}$. FN and SM candidates were separated via their different correlation time distributions. The observed

TABLE 9: Summary of observed IBD candidates, with corresponding signal and background predictions for each integration period before any oscillation fit results have been applied.

	Reactors both on	One reactor $P_{th} < 20\%$	Total
Livetime (days)	139.27	88.66	227.93
IBD candidates	6088	2161	8249
ν Reactor B1	2910.9	774.6	3685.5
ν Reactor B2	3422.4	1331.7	4754.1
Cosmogenic isotope	174.1	110.8	284.9
Correlated FN and SM	93.3	59.4	152.7
Accidentals	36.4	23.1	59.5
Total prediction	6637.1	2299.7	8936.8

prompt energy spectrum is consistent with a flat continuum between 12 and 30 MeV, which extrapolated to the IBD selection window providing a first estimation of the correlated background rate of ≈ 0.75 events/day. The accuracy of this estimate depends on the validity of the extrapolation of the spectral shape. Several FN and SM analyses were performed using different combinations of IV and OV taggings. The main analysis for the FN estimation relies on IV tagging of the prompt triggers with OV veto applied for the IBD selection. A combined analysis was performed to obtain the total spectrum and the total rate estimation of both FN and SM, (0.67 ± 0.20) events/day summarized, in Table 9.

There are four ways that can be utilized to estimate backgrounds. Each independent background component can be measured by isolating samples and subtracting possible correlations. Second, we can measure each independent background component including spectral information when fitting for θ_{13} oscillations. Third, the total background rate is measured by comparing the observed and expected rates as a function of reactor power. Fourth, we can use the both-reactor-off data to measure both the rate and spectrum. The latter two methods are used currently as cross-checks for the background measurements due to low statistics and are described here. The measured daily rate of IBD candidates as a function of the no-oscillation expected rate for different reactor power conditions is shown in Figure 17. The extrapolation to zero reactor power of the fit to the data yields 2.9 ± 1.1 events per day, in excellent agreement with our background estimate. The overall rate of correlated background events that pass the IBD cuts is independently verified by analyzing 22.5 hours of both-reactors-off data [48]. The expected neutrino signal is < 0.3 residual $\bar{\nu}_e$ events.

Calibration data taken with the ^{252}Cf source were used to check the Monte Carlo prediction for any biases in the neutron selection criteria and estimate their contributions to the systematic uncertainty.

The fraction of neutron captures on gadolinium is evaluated to be 86.5% near the center of the target and to be 1.5% lower than the fraction predicted by simulation. Therefore, the Monte Carlo simulation for the prediction of the number of $\bar{\nu}_e$ events is reduced by factor of 0.985. After the prediction of the fraction of neutron captures on gadolinium is scaled

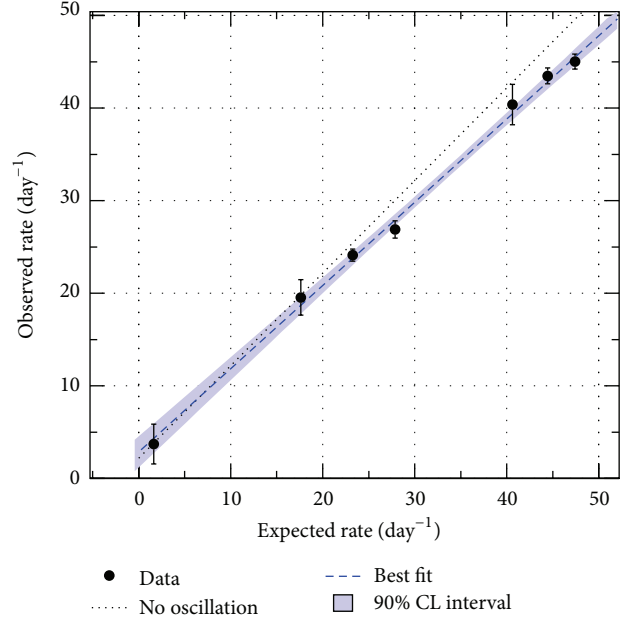


FIGURE 17: Daily number of $\bar{\nu}_e$ candidates as a function of the expected number of $\bar{\nu}_e$. The dashed line shows the fit to the data, along with the 90% C L band. The dotted line shows the expectation in the no-oscillation scenario.

to the data, the prediction reproduces the data within 0.3% under variation of selection criteria.

The ^{252}Cf is also used to check the neutron capture time, ΔT . The simulation reproduces the efficiency (96.2%) of the Δt_{e+n} cut with an uncertainty of 0.5% augmented with sources deployed through the NT and GC.

The efficiency for Gd capture events with visible energy greater than 4 MeV to pass the 6 MeV cut is estimated to be 94.1%. Averaged over the NT, the fraction of neutron captures on Gd accepted by the 6.0 MeV cut is in agreement with calibration data within 0.7%.

The Monte Carlo simulation indicates that the number of IBD events occurring in the GC with the neutron captured in the NT (spill-in) slightly exceeds the number of events occurring in the target with the neutron escaping to the gamma catcher (spill-out), by $1.35\% \pm 0.04\%$ (stat) $\pm 0.30\%$ (sys). The spill-in/out effect is already included in the simulation, and therefore no correction for this is needed. The uncertainty of 0.3% assigned to the net spill-in/out current was quantified by varying the parameters affecting the process, such as gadolinium concentration in the target scintillator and hydrogen fraction in the gamma-catcher fluid within its tolerances. Moreover, the parameter variation was performed with multiple Monte Carlo models at low neutron energies.

5.5. Oscillation Analysis. The oscillation analysis is based on a combined fit to antineutrino rate and spectral shape. The data are compared to the Monte Carlo signal and background events from high-statistics samples. The same selections are applied to both signal and background, with corrections made to Monte Carlo only when necessary to match detector

performance metrics. The oscillation analysis begins by separating the data into 18 variably sized bins between 0.7 and 12.2 MeV. Two integration periods are used in the fit to help separate background and signal fluxes. One set contains data periods, where one reactor is operating at less than 20% of its nominal thermal power, according to power data provided by EDF, while the other set contains data from all other times, typically when both reactors are running. All data end up in one of the two integration periods. Here, we denote the number of observed IBD candidates in each of the bins as N_i , where i runs over the combined 36 bins of both integration periods. The use of multiple periods of data integration takes advantage of the different signal/background ratios in each period, as the signal rate varies with reactor power, while the backgrounds remain constant in time. This technique adds information about background behavior to the fit. The distribution of IBD candidates between the two integration periods is given in Table 9. A prediction of the observed number of signal and background events is constructed for each energy bin, following the same integration period division as the following data:

$$N^{\text{pred}}_{\text{red},i} = \sum_{R=1,2}^{\text{Reactors}} N_i^{\nu,R} + \sum_b^{\text{Bkgnds.}} N_i^b, \quad (17)$$

where $N_i^{\nu,R} = P(\bar{\nu}_e \rightarrow \bar{\nu}_e) N_i^{\text{exp},R}$, $P_{\bar{\nu}_e \rightarrow \bar{\nu}_e}$ is the neutrino survival probability from the well-known oscillation formula, and $N_i^{\text{exp},R}$ is given by (16). The index b runs over the three backgrounds: cosmogenic isotope; correlated; and accidental. The index R runs over the two reactors, Chooz B1 and B2. Background populations were calculated based on the measured rates and the livetime of the detector during each integration period. Predicted populations for both null-oscillation signal and backgrounds may be found in Table 9.

Systematic and statistical uncertainties are propagated to the fit by the use of a covariance matrix M_{ij} in order to properly account for correlations between energy bins. The sources of uncertainty A are listed in Table 10 as follows:

$$M_{ij} = M_{ij}^{\text{sig.}} + M_{ij}^{\text{det.}} + M_{ij}^{\text{stat.}} + M_{ij}^{\text{eff.}} + \sum_b^{\text{Bkgnds.}} M_{ij}^b. \quad (18)$$

Each term $M_{ij}^A = \text{cov}(N_i^{\text{pred}}, N_j^{\text{pred}})_A$ on the right-hand side of (18) represents the covariance of N_i^{pred} and N_j^{pred} due to uncertainty A . The normalization uncertainty associated with each of the matrix contributions may be found from the sum of each matrix; these are summarized in Table 10. Many sources of uncertainty contain spectral shape components which do not directly contribute to the normalization error but do provide for correlated uncertainties between the energy bins. The signal covariance matrix $M_{ij}^{\text{sig.}}$ is calculated taking into account knowledge about the predicted neutrino spectra. The ${}^9\text{Li}$ matrix contribution contains spectral shape uncertainties estimated using different Monte Carlo event generation parameters. The slope of the FN/SM spectrum is allowed to vary from a nearly flat spectrum. Since accidental background uncertainties are measured to a high

TABLE 10: Summary of signal and background normalization uncertainties in this analysis relative to the total prediction.

Source	Uncertainty (%)
Reactor flux	1.67%
Detector response	0.32%
Statistics	1.06%
Efficiency	0.95%
Cosmogenic isotope background	1.38%
FN/SM	0.51%
Accidental background	0.01%
Total	2.66%

precision from many off-time windows, they are included as a diagonal covariance matrix. The elements of the covariance matrix contributions are recalculated as a function of the oscillation and other parameters (see below) at each step of the minimization. This maintains the fractional systematic uncertainties as the bin populations vary from the changes in the oscillation and fit parameters.

A fit of the binned signal and background data to a two-neutrino oscillation hypothesis was performed by minimizing a standard χ^2 function:

$$\chi^2 = \sum_{i,j}^{36} (N_i - N_i^{\text{pred}}) \times (M_{ij})^{-1} (N_j - N_j^{\text{pred}})^T + \frac{(\epsilon_{\text{FN/SM}} - 1)^2}{\sigma_{\text{FN/SM}}^2} + \frac{(\epsilon_{{}^9\text{Li}} - 1)^2}{\sigma_{{}^9\text{Li}}^2} + \frac{(\alpha_E - 1)^2}{\sigma_{\alpha_E}^2} + \frac{(\Delta m_{31}^2 - (\Delta m_{31}^2)_{\text{MINOS}})^2}{\sigma_{\text{MINOS}}^2}. \quad (19)$$

The use of energy spectrum information in this analysis allows additional information on background rates to be gained from the fit, in particular because of the small number of IBD events between 8 and 12 MeV. The two fit parameters $\epsilon_{\text{FN/SM}}$ and $\epsilon_{{}^9\text{Li}}$ are allowed to vary as part of the fit, and they scale the rates of the two backgrounds (correlated and cosmogenic isotopes). The rate of accidentals is not allowed to vary since its initial uncertainty is precisely determined in-situ. The energy scale for predicted signal and ${}^9\text{Li}$ events is allowed to vary linearly according to the α_E parameter with an uncertainty $\sigma_{\alpha_E} = 1.13\%$. A final parameter constrains the mass splitting Δm_{31}^2 using the MINOS measurement [90] of $\Delta m_{31}^2 = (2.32 \pm 0.12) \times 10^{-3} \text{ eV}^2$, where we have symmetrized the error. This error includes the uncertainty introduced by relating the effective mass-squared difference observed in a ν_μ disappearance experiment to the one relevant for reactor experiments and the ambiguity due to the type of the neutrino mass hierarchy; see for example [91]. Uncertainties for these parameters, $\sigma_{\text{FN/SM}}$, $\sigma_{{}^9\text{Li}}$, and σ_{MINOS} , are listed as the initial values in Table 11. The best fit gives $\sin^2 2\theta_{13} = 0.109 \pm 0.030(\text{stat.}) \pm 0.025(\text{syst})$ at $\Delta m_{31}^2 = 2.32 \times 10^{-3} \text{ eV}^2$, with a $\chi^2/\text{NDF} = 42.1/35$. Table 11 gives the resulting values of the fit parameters and their uncertainties. Comparing the

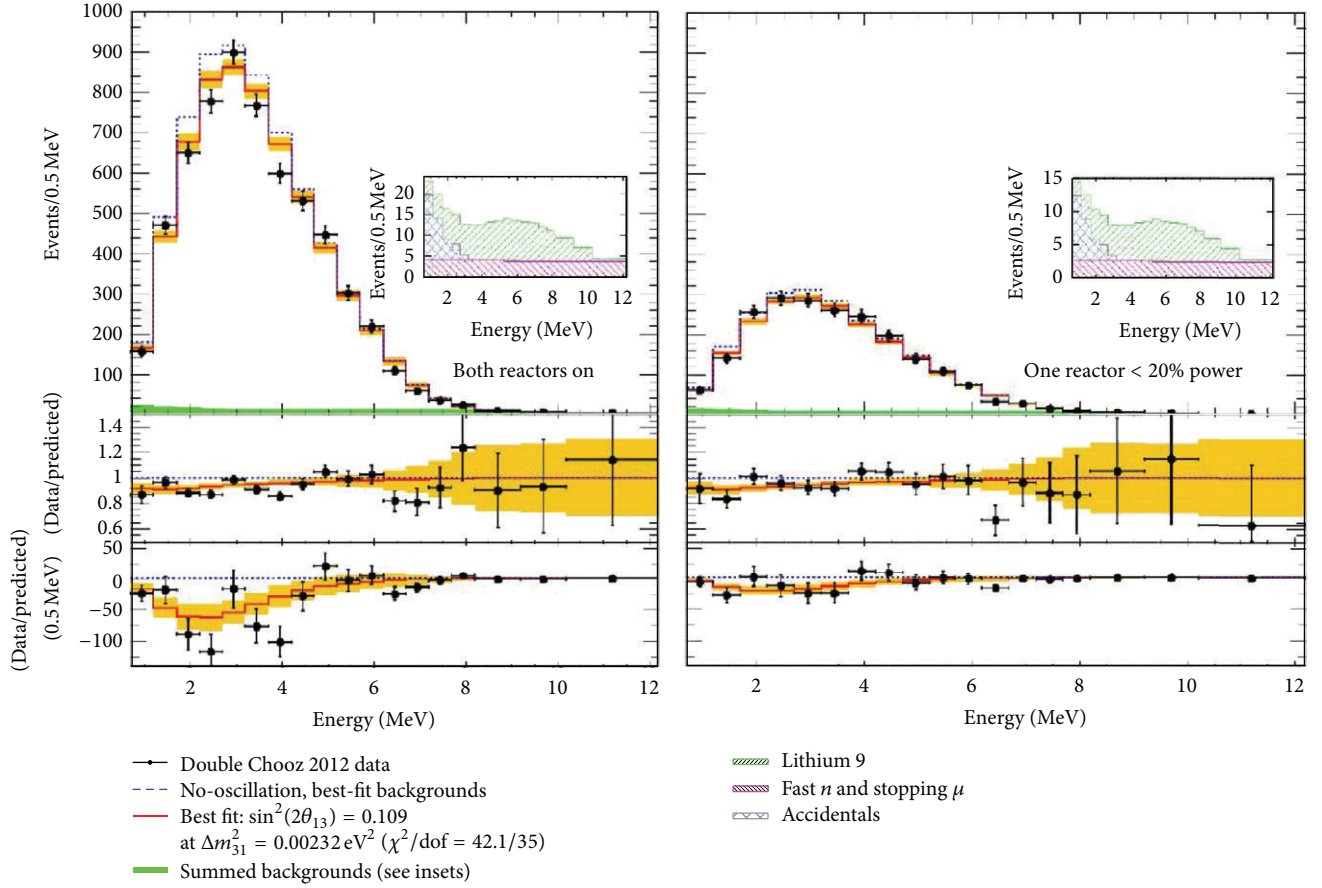


FIGURE 18: Measured prompt energy spectrum for each integration period (data points) superimposed on the expected prompt energy spectrum, including backgrounds (green region), for the no-oscillation (blue dotted curve) and best-fit (red solid curve), backgrounds at $\sin^2 2\theta_{13} = 0.109$ and $\Delta m_{31}^2 = 2.32 \times 10^{-3} \text{ eV}^2$. Inset: stacked spectra of backgrounds. Bottom: differences between data and no-oscillation prediction (data points) and differences between best-fit prediction and no-oscillation prediction (red curve). The orange band represents the systematic uncertainties on the best-fit prediction.

TABLE 11: Parameters in the oscillation fit. Initial values are determined by measurements of background rates or detector calibration data. Best-fit values are outputs of the minimization procedure.

Fit parameter	Initial value	Best-fit value
^9Li Bkg. $\epsilon_{9\text{Li}}$	$(1.25 \pm 0.54) \text{ d}^{-1}$	$(1.00 \pm 0.29) \text{ d}^{-1}$
FN/SM Bkg. $\epsilon_{\text{FN/SM}}$	$(0.67 \pm 0.20) \text{ d}^{-1}$	$(0.64 \pm 0.13) \text{ d}^{-1}$
Energy scale α_E	1.000 ± 0.011	0.986 ± 0.007
Δm_{31}^2 (10^{-3} eV^2)	2.32 ± 0.12	2.32 ± 0.12

values with the ones used as input to the fit in Table 9, we conclude that the background rate and uncertainties are further constrained in the fit, as well as the energy scale.

The final measured spectrum and the best-fit spectrum are shown in Figure 18 for the new and old data sets, and for both together in Figure 19.

An analysis comparing only the total observed number of IBD candidates in each integration period to the expectations produces a best fit of $\sin^2 2\theta_{13} = 0.170 \pm 0.052$ at $\chi^2/\text{NDF} = 0.50/1$. The compatibility probability for the rate-only and rate+shape measurements is about 30% depe-

nding on how the correlated errors are handled between the two measurements.

Confidence intervals for the standard analysis were determined using a frequentist technique [92]. This approach accommodates the fact that the true χ^2 distributions may not be Gaussian and is useful for calculating the probability of excluding the no-oscillation hypothesis. This study compared the data to 10,000 simulations generated at each of 21 test points in the range $0 \leq \sin^2 2\theta_{13} \leq 0.25$. A $\Delta\chi^2$ statistic, equal to the difference between the χ^2 at the test point and the χ^2 at the best fit, was used to determine the region in $\sin^2 2\theta_{13}$ where the $\Delta\chi^2$ of the data was within the given confidence probability. The allowed region at 68% (90%) CL is 0.068 (0.044) $< \sin^2 2\theta_{13} < 0.15$ (0.17). An analogous technique shows that the data exclude the no-oscillation hypothesis at 99.9% (3.1σ).

6. RENO

The reactor experiment for neutrino oscillation (RENO) has obtained a definitive measurement of the smallest neutrino

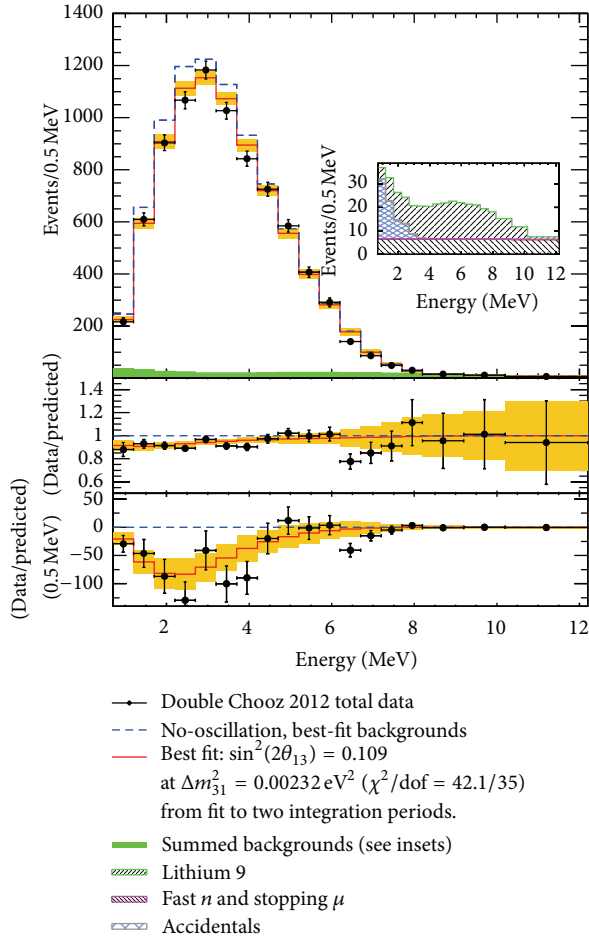


FIGURE 19: Sum of both integration periods plotted in the same manner as Figure 18.

mixing angle of θ_{13} by observing the disappearance of electron antineutrinos emitted from a nuclear reactor, excluding the no-oscillation hypothesis at 4.9σ . From the deficit, the best-fit value of $\sin^2 2\theta_{13}$ is obtained as $0.113 \pm 0.013(\text{stat.}) \pm 0.019(\text{syst.})$ based on a rate-only analysis.

Consideration of RENO began in early 2004, and its proposal was approved by the Ministry of Science and Technology in Korea in May 2005. The company operating the Yonggwang nuclear power plant, KHNP, has allowed us to carry out the experiment in a restricted area. The project started in March 2006. Geological survey was completed in 2007. Civil construction began in middle 2008 and was completed in early 2009. Both near and far detectors are completed in early 2011, and data taking began in early August 2011. RENO is the first experiment to measure θ_{13} with two identical detectors in operation.

6.1. Experimental Setup and Detection Method. RENO detects antineutrinos from six reactors at Yonggwang Nuclear Power Plant in Korea. A symmetric arrangement of the reactors and the detectors, as shown in Figure 20, is useful for minimizing the complexity of the measurement. The

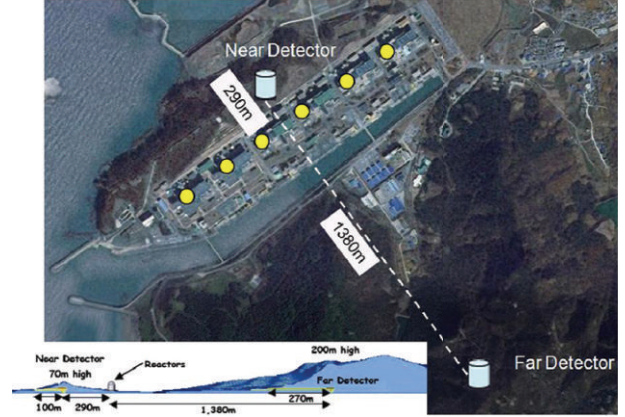


FIGURE 20: A schematic setup of the RENO experiment.

six pressurized water reactors with each maximum thermal output of $2.8 \text{ GW}_{\text{th}}$ (reactors 3, 4, 5, and 6) or $2.66 \text{ GW}_{\text{th}}$ (reactors 1 and 2) are lined up in roughly equal distances and span $\sim 1.3 \text{ km}$.

Two identical antineutrino detectors are located at 294 m and 1383 m, respectively, from the center of reactor array to allow a relative measurement through a comparison of the observed neutrino rates. The near detector is located inside a restricted area of the nuclear power plant, quite close to the reactors to make an accurate measurement of the antineutrino fluxes before their oscillations. The far (near) detector is beneath a hill that provides 450 m (120 m) of water-equivalent rock overburden to reduce the cosmic backgrounds.

The measured far-to-near ratio of antineutrino fluxes can considerably reduce systematic errors coming from uncertainties in the reactor neutrino flux, target mass, and detection efficiency. The relative measurement is independent of correlated uncertainties and helps to minimize uncorrelated reactor uncertainties.

The positions of two detectors and six reactors are surveyed with GPS and total station to determine the baseline distances between detector and reactor to an accuracy of less than 10 cm. The accurate measurement of the baseline distances finds the reduction of reactor neutrino fluxes at detector to a precision of much better than 0.1%. The reactor-flux-weighted baseline is 408.56 m for the near detector and 1443.99 m for the far detector.

6.2. Detector. Each RENO detector (Figure 21) consists of a main inner detector (ID) and an outer veto detector (OD). The main detector is contained in a cylindrical stainless steel vessel that houses two nested cylindrical acrylic vessels. The innermost acrylic vessel holds 18.6 m^3 (16.5 t) $\sim 0.1\%$ Gadolinium-(Gd-) doped liquid scintillator (LS) as a neutrino target. An electron antineutrino can interact with a free proton in LS, $\bar{\nu}_e + p \rightarrow e^+ + n$. The coincidence of a prompt positron signal and a delayed signal from neutron capture by Gd provides the distinctive signature of inverse β decay.

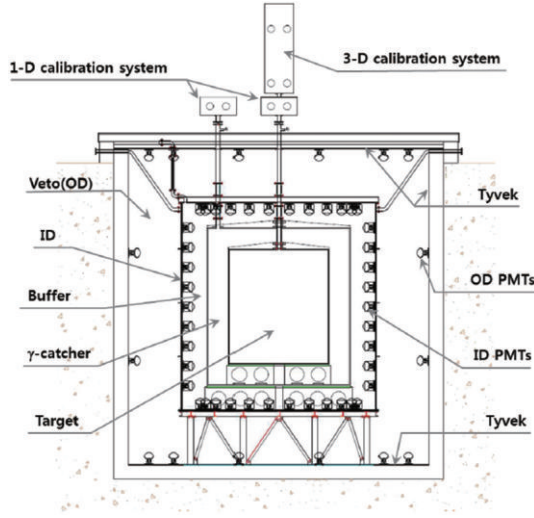


FIGURE 21: A schematic view of the RENO detector. The near and far detectors are identical.

The central target volume is surrounded by a 60 cm thick layer of LS without Gd, useful for catching γ -rays escaping from the target region and thus increasing the detection efficiency. Outside this γ -catcher, a 70 cm thick buffer layer of mineral oil provides shielding from radioactivity in the surrounding rocks and in the 354 10-inch photomultipliers (PMTs) that are mounted on the inner wall of the stainless steel container.

The outermost veto layer of OD consists of 1.5 m of highly purified water in order to identify events coming from outside by their Cherenkov radiation and to shield against ambient γ -rays and neutrons from the surrounding rocks.

The LS is developed and produced as a mixture of linear alkyl benzene (LAB), PPO, and bis-MSB. A Gd-carboxylate complex using TMHA was developed for the best Gd loading efficiency into LS and its long-term stability. Gd-LS and LS are made and filled into the detectors carefully to ensure that the near and far detectors are identical.

6.3. Data Sample. In the 229 day data-taking period between 11 August 2011 to 26 March 2012, the far (near) detector observed 17102 (154088) electron antineutrino candidate events or 77.02 ± 0.59 (800.8 ± 2.0) events/day with a background fraction of 5.5% (2.7%). During this period, all six reactors were mostly on at full power, and reactors 1 and 2 were off for a month each because of fuel replacement.

Event triggers are formed by the number of PMTs with signals above a ~ 0.3 photoelectron (pe) threshold (NHIT). An event is triggered and recorded if the ID NHIT is larger than 90, corresponding to 0.5–0.6 MeV well below the 1.02 MeV as the minimum energy of an IBD positron signal or if the OD NHIT is larger than 10.

The event energy is measured based on the total charge (Q_{tot}) in pe, collected by the PMTs and corrected for gain variation. The energy calibration constant of 250 pe per MeV is determined by the peak energies of various radioactive sources deployed at the center of the target.

TABLE 12: Event rates of the observed candidates and the estimated background.

Detector	Near	Far
Selected events	154088	17102
Total background rate (per day)	21.75 ± 5.93	4.24 ± 0.75
IBD rate after background subtraction (per day)	779.05 ± 6.26	72.78 ± 0.95
DAQ Livetime (days)	192.42	222.06
Detection efficiency (ϵ)	0.647 ± 0.014	0.745 ± 0.014
Accidental rate (per day)	4.30 ± 0.06	0.68 ± 0.03
${}^9\text{Li}/{}^8\text{He}$ rate (per day)	12.45 ± 5.93	2.59 ± 0.75
Fast neutron rate (per day)	5.00 ± 0.13	0.97 ± 0.06

6.4. Background. In the final data samples, uncorrelated (accidentals) and correlated (fast neutrons from outside of ID, stopping muon followers and β - n emitters from ${}^9\text{Li}/{}^8\text{He}$) background events survive selection requirements. The total background rate is estimated to be 21.75 ± 5.93 (near) or 4.24 ± 0.75 (far) events per day and summarized in Table 12.

The uncorrelated background is due to accidental coincidences from random association of a prompt-like event due to radioactivity and a delayed-like neutron capture. The remaining rate in the final sample is estimated to be 4.30 ± 0.06 (near) or 0.68 ± 0.03 (far) events per day.

The ${}^9\text{Li}/{}^8\text{He}$ β - n emitters are mostly produced by energetic muons because their production cross-sections in carbon increase with muon energy. The background rate in the final sample is obtained as 12.45 ± 5.93 (near) or 2.59 ± 0.75 (far) events per day from a fit to the delay time distribution with an observed mean decay time of ~ 250 ms.

An energetic neutron entering the ID can interact in the target to produce a recoil proton before being captured on Gd. Fast neutrons are produced by cosmic muons traversing the surrounding rock and the detector. The estimated fast neutron background is 5.00 ± 0.13 (near) or 0.97 ± 0.06 (far) events per day.

6.5. Systematic Uncertainty. The combined absolute uncertainty of the detection efficiency is correlated between the two detectors and estimated to be 1.5%. Uncorrelated relative detection uncertainties are estimated by comparing the two identical detectors. They come from relative differences between the detectors in energy scale, target protons, Gd capture ratio, and others. The combined uncorrelated detection uncertainty is estimated to be 0.2%.

The uncertainties associated with thermal power and relative fission fraction contribute to 0.9% of the $\bar{\nu}_e$ yield per core to the uncorrelated uncertainty. The uncertainties associated with $\bar{\nu}_e$ yield per fission, fission spectra, and thermal energy released per fission result in a 2.0% correlated uncertainty. We assume a negligible contribution of the spent fuel to the uncorrelated uncertainty.

6.6. Results. All reactors were mostly in steady operation at the full power during the data-taking period, except for reactor 2 (R2), which was off for the month of September 2011,

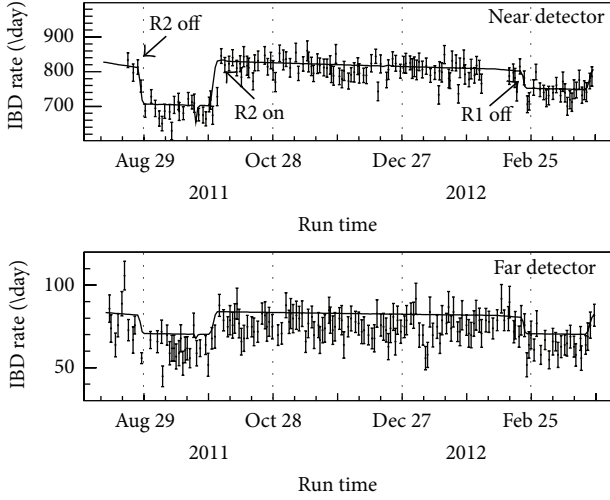


FIGURE 22: Measured daily-average rates of reactor neutrinos after background subtraction in the near and far detectors as a function of running time. The solid curves are the predicted rates for no oscillation.

and reactor 1 (R1), which was off from February 23 2012 for fuel replacement. Figure 22 presents the measured daily rates of IBD candidates after background subtraction in the near and far detectors. The expected rates assuming no oscillation, obtained from the weighted fluxes by the thermal power and the fission fractions of each reactor and its baseline to each detector, are shown for comparison.

Based on the number of events at the near detector and assuming no oscillation, RENO finds a clear deficit, with a far-to-near ratio

$$R = 0.920 \pm 0.009 \text{ (stat.)} \pm 0.014 \text{ (syst.)}. \quad (20)$$

The value of $\sin^2 2\theta_{13}$ is determined from a χ^2 fit with pull terms on the uncorrelated systematic uncertainties. The number of events in each detector after the background subtraction has been compared with the expected number of events, based on the reactor neutrino flux, detection efficiency, neutrino oscillations, and contribution from the reactors to each detector determined by the baselines and reactor fluxes.

The best-fit value thus obtained is

$$\sin^2 2\theta_{13} = 0.113 \pm 0.013 \text{ (stat.)} \pm 0.019 \text{ (syst.)}, \quad (21)$$

and it excludes the no-oscillation hypothesis at the 4.9 standard deviation level.

RENO has observed a clear deficit of 8.0% for the far detector and of 1.2% for the near detector, concluding a definitive observation of reactor antineutrino disappearance consistent with neutrino oscillations. The observed spectrum of IBD prompt signals in the far detector is compared to the non oscillation expectations based on measurements in the near detector in Figure 23. The spectra of prompt signals are obtained after subtracting backgrounds shown in the inset. The disagreement of the spectra provides further evidence of neutrino oscillation.

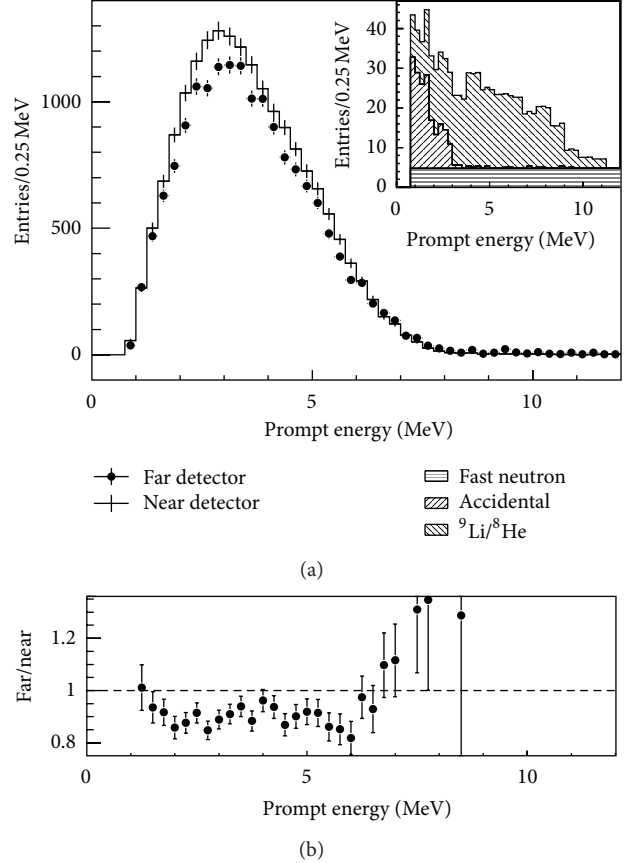


FIGURE 23: Observed spectrum of the prompt signals in the far detector compared with the nonoscillation predictions from the measurements in the near detector. The backgrounds shown in the inset are subtracted for the far spectrum. The background fraction is 5.5% (2.7%) for far (near) detector. Errors are statistical uncertainties only. (b) The ratio of the measured spectrum of far detector to the non-oscillation prediction.

In summary, RENO has observed reactor antineutrinos using two identical detectors each with 16 tons of Gd-loaded liquid scintillator and a 229 day exposure to six reactors with total thermal energy of 16.5 GW_{th}. In the far detector, a clear deficit of 8.0% is found by comparing a total of 17102 observed events with an expectation based on the near detector measurement assuming no oscillation. From this deficit, a rate-only analysis obtains $\sin^2 2\theta_{13} = 0.113 \pm 0.013 \text{ (stat.)} \pm 0.019 \text{ (syst.)}$. The neutrino mixing angle θ_{13} is measured with a significance of 4.9 standard deviation.

6.7. Future Prospects and Plan. RENO has measured the value of $\sin^2 2\theta_{13}$ with a total error of ± 0.023 . The expected sensitivity of RENO is to obtain ± 0.01 for the error based on the three years of data, leading to a statistical error of 0.006 and a systematic error of ~ 0.005 .

The fast neutron and $^9\text{Li}/^8\text{He}$ backgrounds produced by cosmic muons depend on the detector sites having different overburdens. Therefore, their uncertainties are the largest

contribution to the uncorrelated error in the current result, and change the systematic error by 0.017 at the best-fit value.

RENO makes efforts on further reduction of backgrounds, especially by removing the $^9\text{Li}/^8\text{He}$ background by a tighter muon veto requirement and a spectral shape analysis to improve the systematic error. A longer-term effort will be made to reduce the systematic uncertainties of reactor neutrino flux and detector efficiency.

7. The Reactor Antineutrino Anomaly-Thierry

7.1. New Predicted Cross-Section per Fission. Fission reactors release about $10^{20} \bar{\nu}_e \text{ GW}^{-1}\text{s}^{-1}$, which mainly come from the beta decays of the fission products of ^{235}U , ^{238}U , ^{239}Pu , and ^{241}Pu . The emitted antineutrino spectrum is then given by $S_{\text{tot}}(E_\nu) = \sum_k f_k S_k(E_\nu)$, where f_k refers to the contribution of the main fissile nuclei to the total number of fissions of the k th branch and S_k to their corresponding neutrino spectrum per fission. Antineutrino detection is achieved via the inverse beta-decay (IBD) reaction $\bar{\nu}_e + {}^1\text{H} \rightarrow e^+ + n$. Experiments at baselines below 100 m reported either the ratios (R) of the measured to predicted cross-section per fission, or the observed event rate to the predicted rate.

The event rate at a detector is predicted based on the following formula:

$$N_\nu^{\text{Pred}}(s^{-1}) = \frac{1}{4\pi L^2} N_p \frac{P_{\text{th}}}{\langle E_f \rangle} \sigma_f^{\text{pred}}, \quad (22)$$

where the first term stands for the mean solid angle and N_p is the number of target protons for the inverse beta-decay process of detection. These two detector-related quantities are usually known with very good accuracy. The last two terms come from the reactor side. The ratio of P_{th} , the thermal power of the reactor, over $\langle E_f \rangle$, the mean energy per fission, provide the mean number of fissions in the core. P_{th} can be known at the subpercent level in commercial reactors, somewhat less accurately at research reactors. The mean energy per fission is computed as the average over the four main fissioning isotopes, accounting for 99.5% of the fissions

$$\langle E_f \rangle = \sum_k \langle E_k \rangle, \quad k = {}^{235}\text{U}, {}^{238}\text{U}, {}^{239}\text{Pu}, {}^{241}\text{Pu}. \quad (23)$$

It is accurately known from the nuclear databases and study of all decays and neutron captures subsequent to a fission [72]. Finally, the dominant source of uncertainty and by far the most complex quantity to compute is the mean cross-section per fission defined as

$$\sigma_f^{\text{pred}} = \int_0^\infty S_{\text{tot}}(E_\nu) \sigma_{V-A}(E_\nu) dE_\nu = \sum_k f_k \sigma_{f,k}^{\text{pred}}, \quad (24)$$

where the $\sigma_{f,k}^{\text{pred}}$ is the predicted cross-sections for each fissile isotope, S_{tot} is the model dependent reactor neutrino

spectrum for a given average fuel composition (f_k), and σ_{V-A} is the theoretical cross-section of the IBD reaction:

$$\sigma_{V-A}(E_e) [\text{cm}^2] = \frac{857 \times 10^{-43}}{\tau_n [\text{s}]} p_e [\text{MeV}] \times E_e [\text{MeV}] (1 + \delta_{\text{rec}} + \delta_{\text{wm}} + \delta_{\text{rad}}), \quad (25)$$

where δ_{rec} , δ_{wm} , and δ_{rad} are, respectively, the nucleon recoil, weak magnetism, and radiative corrections to the cross-section (see [22, 93] for details). The fraction of fissions undergone by the k th isotope, f_k , can be computed at the few percent level with reactor evolution codes (see for instance [79]), but their impact in the final error is well reduced by the sum rule of the total thermal power, accurately known from independent measurements

Accounting for new reactor antineutrino spectra [32] the normalization of predicted antineutrino rates, $\sigma_{f,k}^{\text{pred}}$, is shifted by +3.7%, +4.2%, +4.7%, and +9.8% for $k = {}^{235}\text{U}$, ^{239}Pu , ^{241}Pu , and ^{238}U , respectively. In the case of ^{238}U , the completeness of nuclear databases over the years largely explains the +9.8% shift from the reference computations [22].

The new predicted cross-section for any fuel composition can be computed from (24). By default, the new computation takes into account the so-called off-equilibrium correction [22] of the antineutrino fluxes (increase in fluxes caused by the decay of long-lived fission products). Individual cross-sections per fission per fissile isotope are slightly different, by +1.25% for the averaged composition of Bugey-4 [10], with respect to the original publication of the reactor antineutrino anomaly [93] because of the slight upward shift of the antineutrino flux consecutive to the work of [32] (see Section 2.2 for details).

7.2. Impact of the New Reactor Neutrino Spectra on Past Short-Baseline (<100 m) Experimental Results. In the eighties and nineties, experiments were performed with detectors located a few tens of meters from nuclear reactor cores at ILL, Goesgen, Rovno, Krasnoyarsk, Bugey (phases 3 and 4), and Savannah River [7–15]. In the context of the search of $\mathcal{O}(\text{eV})$ sterile neutrinos, these experiments, with baselines below 100 m, have the advantage that they are not sensitive to a possible θ_{13} , Δm_{31}^2 -driven oscillation effect (unlike the Palo Verde and CHOOZ experiments, for instance).

The ratios of observed event rates to predicted event rates (or cross-section per fission), $R = N_{\text{obs}}/N_{\text{pred}}$, are summarized in Table 13. The observed event rates and their associated errors are unchanged with respect to the publications; the predicted rates are reevaluated separately in each experimental case. One can observe a general systematic shift more or less significantly below unity. These reevaluations unveil a new *reactor antineutrino anomaly* (http://irfu.cea.fr/en/Phoce/Vie_des_labos/Ast/ast_visu.php?id_ast=3045) [93], clearly illustrated in Figure 24. In order to quantify the statistical significance of the anomaly, one can compute the weighted average of the ratios of expected-over-predicted rates, for all short-baseline

Gaussian, but with slightly longer tails, which were taken into account in the calculations (in contours that appear later, error bars are enlarged). With the old antineutrino spectra, the mean ratio is $\mu = 0.980 \pm 0.024$.

With the new antineutrino spectra, one obtains $\mu = 0.927 \pm 0.023$, and the fraction of simple Monte Carlo experiments with $r \geq 1$ is 0.3%, corresponding to a -2.9σ effect (while a simple calculation assuming normality would lead to -3.2σ). Clearly, the new spectra induce a statistically significant deviation from the expectation. This motivates the definition of an experimental cross-section $\sigma_f^{\text{ano},2012} = 0.927 \times \sigma_f^{\text{pred,new}}$. With the new antineutrino spectra, the minimum χ^2 for the data sample is $\chi_{\text{min,data}}^2 = 18.4$. The fraction of simple Monte Carlo experiments with $\chi_{\text{min,data}}^2 < \chi_{\text{min,data}}^2$ is 50%, showing that the distribution of experimental ratios in \vec{R} around the mean value is representative given the correlations.

Assuming the correctness of $\sigma_f^{\text{pred,new}}$, the anomaly could be explained by a common bias in all reactor neutrino experiments. The measurements used different detection techniques (scintillator counters and integral detectors). Neutrons were tagged either by their capture in metal-loaded scintillator, or in proportional counters, thus leading to two distinct systematics. As far as the neutron detection efficiency calibration is concerned, note that different types of radioactive sources emitting MeV or sub-MeV neutrons were used (Am-Be, ^{252}Cf , Sb-Pu, and Pu-Be). It should be mentioned that the Krasnoyarsk, ILL, and SRP experiments operated with nuclear fuel such that the difference between the real antineutrino spectrum and that of pure ^{235}U was less than 1.5%. They reported similar deficits to those observed at other reactors operating with a mixed fuel. Hence, the anomaly can be associated neither with a single fissile isotope nor with a single detection technique. All these elements argue against a trivial bias in the experiments, but a detailed analysis of the most sensitive of them, involving experts, would certainly improve the quantification of the anomaly.

The other possible explanation of the anomaly is based on a real physical effect and is detailed in the next section. In that analysis, shape information from the Bugey-3 and ILL-published data [7, 8] is used. From the analysis of the shape of their energy spectra at different source-detector distances [8, 9], the Goesgen and Bugey-3 measurements exclude oscillations with $0.06 < \Delta m^2 < 1 \text{ eV}^2$ for $\sin^2(2\theta) > 0.05$. Bugey-3's 40 m/15 m ratio data from [8] is used as it provides the best limit. As already noted in [94], the data from ILL showed a spectral deformation compatible with an oscillation pattern in their ratio of measured over predicted events. It should be mentioned that the parameters best fitting the data reported by the authors of [94] were $\Delta m^2 = 2.2 \text{ eV}^2$ and $\sin^2(2\theta) = 0.3$. A reanalysis of the data of [94] was carried out in order to include the ILL shape-only information in the analysis of the reactor antineutrino anomaly. The contour in Figure 14 of [7] was reproduced for the shape-only analysis (while for the rate-only analysis discussed above that of [94] was reproduced, excluding the no-oscillation hypothesis at 2σ).

7.3. The Fourth Neutrino Hypothesis (3 + 1 Scenario)

7.3.1. Reactor Rate-Only Analysis. The reactor antineutrino anomaly could be explained through the existence of a fourth nonstandard neutrino, corresponding in the flavor basis to a sterile neutrino ν_s with a large Δm_{new}^2 value.

For simplicity, the analysis presented here is restricted to the 3 + 1 four-neutrino scheme in which there is a group of three active neutrino masses separated from an isolated neutrino mass, such that $|\Delta m_{\text{new}}^2| \gg 10^{-2} \text{ eV}^2$. The latter would be responsible for very short-baseline reactor neutrino oscillations. For energies above the IBD threshold and baselines below 100 m, the approximated oscillation formula

$$P_{ee} = 1 - \sin^2(2\theta_{\text{new}}) \sin^2\left(\frac{\Delta m_{\text{new}}^2 L}{4E_{\bar{\nu}_e}}\right) \quad (26)$$

is adopted, where active neutrino oscillation effects are neglected at these short baselines. In such a framework, the mixing angle is related to the U matrix element by the relation:

$$\sin^2(2\theta_{\text{new}}) = 4|U_{e4}|^2(1 - |U_{e4}|^2). \quad (27)$$

One can now fit the sterile neutrino hypothesis to the data (baselines below 100 m) by minimizing the least-squares function

$$(P_{ee} - \vec{R})^T W^{-1} (P_{ee} - \vec{R}), \quad (28)$$

assuming $\sin^2(2\theta_{13}) = 0$. Figure 25 provides the results of the fit in the $\sin^2(2\theta_{\text{new}}) - \Delta m_{\text{new}}^2$ plane, including only the reactor experiment rate information. The fit to the data indicates that $|\Delta m_{\text{new,R}}^2| > 0.2 \text{ eV}^2$ (99%) and $\sin^2(2\theta_{\text{new,R}}) \sim 0.14$. The best-fit point is at $|\Delta m_{\text{new,R}}^2| = 0.5 \text{ eV}^2$ and $\sin^2(2\theta_{\text{new,R}}) \sim 0.14$. The no-oscillation analysis is excluded at 99.8%, corresponding roughly to 3σ .

7.3.2. Reactor Rate+Shape Analysis. The ILL experiment may have seen a hint of oscillation in their measured positron energy spectrum [7, 94], but Bugey-3's results do not point to any significant spectral distortion more than 15 m away from the antineutrino source. Hence, in a first approximation, hypothetical oscillations could be seen as an energy-independent suppression of the $\bar{\nu}_e$ rate by a factor of $(1/2)\sin^2(2\theta_{\text{new,R}})$, thus leading to $\Delta m_{\text{new,R}}^2 > 1 \text{ eV}^2$ and accounting for the Bugey-3 and Goesgen shape analyses [8, 9]. Considering the weighted average of all reactor experiments, one obtains an estimate of the mixing angle, $\sin^2(2\theta_{\text{new,R}}) \sim 0.15$. The ILL positron spectrum is thus in agreement with the oscillation parameters found independently in the reanalyses mainly based on rate information. Because of the differences in the systematic effects in the rate and shape analyses, this coincidence is in favor of a true physical effect rather than an experimental anomaly. Including the finite spatial extension of the nuclear reactors and the ILL and Bugey-3 detectors, it is found that the small dimensions of the ILL nuclear core lead to small corrections of the oscillation pattern imprinted on the positron spectrum.

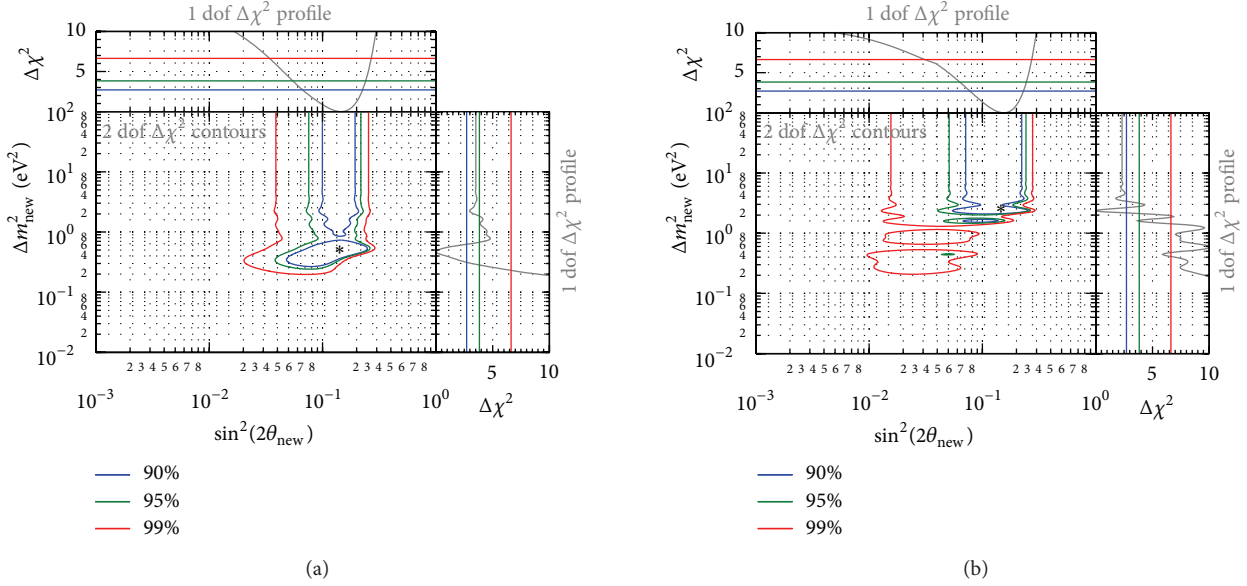


FIGURE 25: (a) Allowed regions in the $\sin^2(2\theta_{\text{new}}) - \Delta m^2_{\text{new}}$ plane obtained from the fit of the reactor neutrino data, without any energy spectra information, to the 3 + 1 neutrino hypothesis, with $\sin^2(2\theta_{13}) = 0$. The best-fit point is indicated by a star. (b) Allowed regions in the $\sin^2(2\theta_{\text{new}}) - \Delta m^2_{\text{new}}$ plane obtained from the fit of the reactor neutrino data, without ILL-shape information, but with the stringent oscillation constraint of Bugey-3 based on the 40 m/15 m ratios to the 3 + 1 neutrino hypothesis, with $\sin^2(2\theta_{13}) = 0$. The best-fit point is indicated by a star.

However, the large extension of the Bugey nuclear core is sufficient to wash out most of the oscillation pattern at 15 m. This explains the absence of shape distortion in the Bugey-3 experiment. We now present results from a fit of the sterile neutrino hypothesis to the data including both Bugey-3 and ILL original results (no-oscillation reported). With respect to the rate only parameters, the solutions at lower $|\Delta m^2_{\text{new},R+S}|$ are now disfavored at large mixing angle because they would have imprinted a strong oscillation pattern in the energy spectra (or their ratio) measured at Bugey-3 and ILL. The best fit point is moved to $|\Delta m^2_{\text{new},R+S}| = 2.4 \text{ eV}^2$, whereas the mixing angle remains almost unchanged, at $\sin^2(2\theta_{\text{new},R+S}) \sim 0.14$. The no-oscillation hypothesis is excluded at 99.6%, corresponding roughly to 2.9σ . Figure 25 provides the results of the fit in the $\sin^2(2\theta_{\text{new}}) - \Delta m^2_{\text{new}}$ plane, including both the reactor experiment rate and shape (Bugey-3 and ILL) data.

7.4. Combination of the Reactor and the Gallium Anomalies. It is also possible to combine the results on the reactor antineutrino anomaly with the results on the gallium anomaly. The goal is to quantify the compatibility of the reactor and the gallium data.

For the reanalysis of the Gallex and Sage calibration runs with ⁵¹Cr and ³⁷Ar radioactive sources emitting $\sim 1 \text{ MeV}$ electron neutrinos [95–100], the methodology developed in [101] is used. However, in the analysis shown here, possible correlations between these four measurements are included. Details are given in [93]. This has the effect of being slightly more conservative, with the no-oscillation hypothesis disfavored at 97.7% C.L. Gallex and Sage observed an average deficit of $R_G = 0.86 \pm 0.06$ (1σ). The best-fit point is at

$|\Delta m^2_{\text{gallium}}| = 2.4 \text{ eV}^2$ (poorly defined), whereas the mixing angle is found to be $\sin^2(2\theta_{\text{gallium}}) \sim 0.27 \pm 0.13$. Note that the best-fit values are very close to those obtained by the analysis of the rate+shape reactor data.

Combining both the reactor and the gallium data, The no-oscillation hypothesis is disfavored at 99.97% C.L. (3.6σ). Allowed regions in the $\sin^2(2\theta_{\text{new}}) - \Delta m^2_{\text{new}}$ plane are displayed in Figure 26, together with the marginal $\Delta\chi^2$ profiles for $|\Delta m^2_{\text{new}}|$ and $\sin^2(2\theta_{\text{new}})$. The combined fit leads to the following constraints on oscillation parameters: $|\Delta m^2_{\text{new}}| > 1.5 \text{ eV}^2$ (99% C.L.) and $\sin^2(2\theta_{\text{new}}) = 0.17 \pm 0.04$ (1σ). The most probable $|\Delta m^2_{\text{new}}|$ is now rather better defined with respect to what has been published in [93], at $|\Delta m^2_{\text{new}}| = 2.3 \pm 0.1 \text{ eV}^2$.

7.5. Status of the Reactor Antineutrino Anomaly. The impact of the new reactor antineutrino spectra has been extensively studied in [93]. The increase of the expected antineutrino rate by about 4.5% combined with revised values of the antineutrino cross-section significantly decreased the normalized ratio of observed-to-expected event rates in all previous reactor experiments performed over the last 30 years at distances below 100 m [7–15]. The new average ratio, updated early 2012, is now 0.927 ± 0.023 , leading to an enhancement of reactor antineutrino anomaly, now significant at the 3σ confidence level. The best-fit point is at $|\Delta m^2_{\text{new},R+S}| = 2.4 \text{ eV}^2$ whereas the mixing angle is at $\sin^2(2\theta_{\text{new},R+S}) \sim 0.14$.

This deficit could still be due to some unknown in the reactor physics, but it can also be analyzed in terms of a suppression of the $\bar{\nu}_e$ rate at short distance as could be

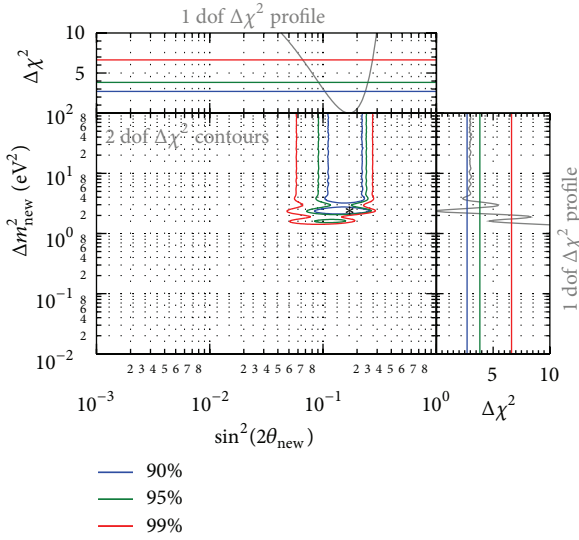


FIGURE 26: Allowed regions in the $\sin^2(2\theta_{\text{new}}) - \Delta m^2_{\text{new}}$ plane from the combination of reactor neutrino experiments, the Gallex and Sage calibration sources experiments, and the ILL and Bugey-3-energy spectra. The data are well fitted by the $3 + 1$ neutrino hypothesis, while the no-oscillation hypothesis is disfavored at 99.97% C.L. (3.6σ).

expected from a sterile neutrino, beyond the standard model, with a large $|\Delta m^2_{\text{new}}| \gg |\Delta m^2_{31}|$. Note that hints of such results were already present at the ILL neutrino experiment in 1981 [94].

Considering the reactor $\bar{\nu}_e$ anomaly and the gallium ν_e source experiments [95–101] together, it is interesting to note that in both cases (neutrinos and antineutrinos) comparable deficits are observed at a similar L/E . Furthermore, it turns out that each experiment fitted separately leads to similar values of $\sin^2(2\theta_{\text{new}})$ and similar lower bounds for $|\Delta m^2_{\text{new}}|$ but without a strong significance. A combined global fit of gallium data and of short-baseline reactor data, taking into account the reevaluation of the reactor results discussed here, as well as the existing correlations, leads to a solution for a new neutrino oscillation, such that $|\Delta m^2_{\text{new}}| > 1.5 \text{ eV}^2$ (99% C.L.) and $\sin^2(2\theta_{\text{new}}) = 0.17 \pm 0.04$ (1σ), disfavoring the no-oscillation case at 99.97% C.L. (3.6σ). The most probable $|\Delta m^2_{\text{new}}|$ is now at $|\Delta m^2_{\text{new}}| = 2.3 \pm 0.1 \text{ eV}^2$. This hypothesis should be checked against systematical effects, either in the prediction of the reactor antineutrino spectra or in the experimental results.

8. Reactor Monitoring for Nonproliferation of Nuclear Weapons

In the past, neutrino experiments have only been used for fundamental research, but today, thanks to the extraordinary progress of the field, for example, the measurement of the oscillation parameters, neutrinos could be useful for society.

The International Atomic Energy Agency (IAEA) works with its member states to promote safe, secure, and peaceful nuclear technologies. One of its missions is to verify that

safeguarded nuclear material and activities are not used for military purposes. In a context of international tension, neutrino detectors could help the IAEA to verify the treaty on the non-proliferation of nuclear weapons (NPT), signed by 145 states around the world.

A small neutrino detector located at a few tens of meters from a nuclear core could monitor nuclear reactor cores non-intrusively, robustly, and automatically. Since the antineutrino spectra and relative yields of fissioning isotopes ^{235}U , ^{238}U , ^{239}Pu , and ^{241}Pu depend on the isotopic composition of the core, small changes in composition could be observed without ever directly accessing the core itself. Information from a modest-sized antineutrino detector, coupled with the well-understood principles that govern the core's evolution in time, can be used to determine whether the reactor is being operated in an illegitimate way. Furthermore, such a detector can help to improve the reliability of the operation, by providing an independent and accurate measurement, in real time, of the thermal power and its reactivity at a level of a few percent. The intention is to design an “optimal” monitoring detector by using the experience obtained from neutrino physics experiments and feasibility studies.

Sands is a one cubic meter antineutrino detector located at 25 meters from the core of the San Onofre reactor site in California [102]. The detector has been operating for several months in an automatic and nonintrusive fashion that demonstrates the principles of reactor monitoring. Although the signal-to-noise ratio of the current design is still less than two, it is possible to monitor the thermal power at a level of a few percent in two weeks. At this stage of the work, the study of the evolution of the fuel seems difficult, but this has already been demonstrated by the Bugey and Rovno experiments.

The NUCIFER experiment in France [103], a 850 liters Gd-doped liquid scintillator detector installed at 7 m from the Osiris nuclear reactor core at CEA-Saclay. The goal is the measurement of its thermal power and plutonium content. The design of such a small volume detector has been focused on high detection efficiency and good background rejection. The detector is being operated to since May 2012, and first results are expected in 2013.

The near detectors of Daya Bay, RENO, and Double Chooz will be a research detector with a very high sensitivity to study neutrino oscillations. Millions of events are being detected in the near detectors (between 300 and 500 m away from the cores). These huge statistics could be exploited to help the IAEA in its safeguards missions. The potential of neutrinos to detect various reactor diversion scenarios can be tested.

A realistic reactor monitor is likely to be somewhere between the two concepts presented above.

9. Future Prospects

Reactors are powerful neutrino sources for free. It is a well understood source since the precision of the neutrino flux and energy spectrum is better than 2%. With a near detector, this uncertainty can be reduced to 0.3%. Clearly, this is much better than usual neutrinos sources such as accelerators, solar, and atmospheric neutrinos. If a detector is placed at different



FIGURE 27: The new site for a long-baseline reactor neutrino experiment.

baseline, an experiment with different motivation can be planned.

9.1. Mass Hierarchy. With the discovery of the unexpected large θ_{13} , mass hierarchy and even the CP phase become accessible with nowadays technologies. A number of new projects are now proposed based on different neutrino sources and different types of detectors.

It is known that neutrino mass hierarchy can be determined by long-baseline (more than 1000 km) accelerator experiment through matter effects. Atmospheric neutrinos may also be used for this purpose using a huge detector. Neutrino mass hierarchy can in fact distort the energy spectrum from reactors [104, 105], and a Fourier transformation of the spectrum can enhance the signature since mass terms appear in the frequency regime of the oscillation probability [106].

It is also shown that by employing a different Fourier transformation as the following:

$$\begin{aligned} \text{FCT}(\omega) &= \int_{t_{\min}}^{t_{\max}} F(t) \cos(\omega t) dt, \\ \text{FST}(\omega) &= \int_{t_{\min}}^{t_{\max}} F(t) \sin(\omega t) dt, \end{aligned} \quad (29)$$

the signature of mass hierarchy is more evident, and it is independent of the precise knowledge of Δ_{23}^2 [107].

The normal hierarchy and inverted hierarchy have very different shapes of the energy spectrum after the Fourier transformation. A detailed Monte Carlo study [108] shows that if $\sin^2 2\theta_{13}$ is more than (1-2)%, a (10-50), kt liquid scintillator at a baseline of about 60 km with an energy resolution better than (2-3)% can determine the mass hierarchy at more than 90% C L. In fact, with $\sin^2 2\theta_{13} = 0.1$, the mass hierarchy can be determined up to the 3σ level with a nominal detector size of 20 kt and a detector energy resolution of 3%.

The group at the Institute of High Energy Physics in Beijing proposed such an experiment in 2008. Fortunately, at a distance of 60 km from Daya Bay, there is a mountain with overburden more than 1500 MWE, where an underground lab can be built. Moreover, this location is 60 km from another nuclear power plant to be built, as shown in Figure 27. The total number of reactors, 6 operational and 6 to be built, may give a total thermal power of more than 35 GW.

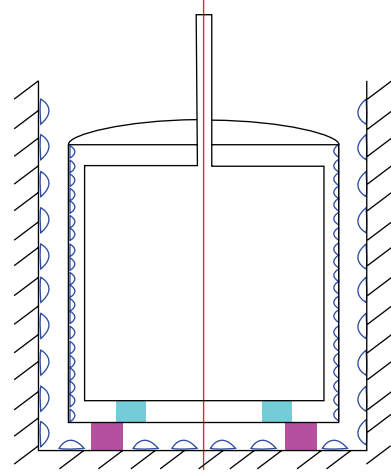


FIGURE 28: A conceptual design of a large liquid scintillator detector.

A conceptual design of the detector is shown in Figure 28. The detector is 30 m in diameter and 30 m high, filled with 20 kt liquid scintillator. The oil buffer will be 6 kt and water buffer is 10 kt. The totally needed number of 20" PMTs is 15000, covering 80% of the surface area.

There are actually two main technical difficulties for such a detector. The attenuation length of the liquid scintillator should be more than 30 m, and the quantum efficiency of PMTs should be more than 40%. R&D efforts are now started at IHEP, and results will be reported in the near future.

There is another proposed project to construct an underground detector of RENO-50 [109]. It consists of 5,000 tons of ultralow-radioactivity liquid scintillator and photomultiplier tubes, located at roughly 50 km away from the Yonggwang nuclear power plant in Korea, where the neutrino oscillation due to θ_{12} takes place at maximum. RENO-50 is expected to detect neutrinos from nuclear reactors, the sun, supernova, the earth, any possible stellar object, and a J-PARC neutrino beam. It could be served as a multipurpose and long-term operational detector including a neutrino telescope. The main goal is to measure the most accurate (1%) value of θ_{12} and to attempt determination of the neutrino mass hierarchy.

9.2. Precision Measurement of Mixing Parameters. A 20 kt liquid scintillator can have a long list of physics goals. In addition to neutrino mass hierarchy, neutrino mixing parameters including θ_{12} , Δm_{12}^2 and Δm_{23}^2 can be measured at the ideal baseline of 60 km to a precision better than 1%. Combined with results from other experiments for θ_{23} and θ_{13} , the unitarity of the neutrino mixing matrix can be tested up to 1% level, much better than that in the quark sector for the CKM matrix. This is very important to explore the physics beyond the standard model, and issues like sterile neutrinos can be studied.

In fact, for this purpose, there is no need to require extremely good energy resolution and huge detectors. Some of the current members of the RENO group indeed proposed a 5 kt liquid scintillator detector exactly for this purpose [109].

If funding is approved, they can start right away based on the existing technology.

9.3. Others. A large liquid scintillator detector is also ideal for supernova neutrinos since it can determine neutrino energies for different flavors, much better than flavor-blind detectors. Geoneutrinos can be another interesting topic, together with other traditional topics such as atmospheric neutrinos, solar neutrinos, and exotic searches.

10. Conclusions and Outlook

Three reactor experiments have definitively measured the value of $\sin^2 2\theta_{13}$ based on the disappearance of electron antineutrinos. Based on unprecedentedly copious data, Daya Bay and RENO have performed rather precise measurements of the value. Averaging the results of the three reactor experiments with the standard Particle Data Group method, one obtains $\sin^2 2\theta_{13} = 0.098 \pm 0.013$ [110]. It took 14 years to measure all three mixing angles after the discovery of neutrino oscillation in 1998.

The exciting result of solving the longstanding secret provides a comprehensive picture of neutrino transformation among three kinds of neutrinos and opens the possibility of searching for CP violation in the lepton sector. The surprisingly large value of θ_{13} will strongly promote the next round of neutrino experiments to find CP violation effects and determine the neutrino mass hierarchy. The relatively large value has already triggered reconsideration of future long-baseline neutrino oscillation experiments. The successful measurement of θ_{13} has made the very first step on the long journey to the complete understanding of the fundamental nature and implications of neutrino masses and mixing parameters.

References

- [1] W. Pauli Jr., Address to Group on Radioactivity (Tuebingen, 1930) (Unpublished) Septieme conseil de physique Solvay, Bruxelles, 1033 (Gautier-Villars, Paris, France, 1934).
- [2] E. Fermi, "Versuch einer theorie der β -strahlen. I," *Zeitschrift für Physik*, vol. 88, no. 3-4, pp. 161–177, 1934.
- [3] F. Reines and C. L. Cowan Jr., "Detection of the free neutrino," *Physical Review*, vol. 92, no. 3, pp. 830–831, 1953.
- [4] C. L. Cowan Jr., F. Reines, F. B. Harrison, H. W. Kruse, and A. D. McGuire, "Detection of the free neutrino: a confirmation," *Science*, vol. 124, no. 3212, pp. 103–104, 1956.
- [5] F. Reines, C. L. Cowan Jr., F. B. Harrison, A. D. McGuire, and H. W. Kruse, "Detection of the free antineutrino," *Physical Review*, vol. 117, no. 1, pp. 159–173, 1960.
- [6] F. Reines and C. L. Cowan Jr., "Free antineutrino absorption cross section. I. Measurement of the free antineutrino absorption cross section by protons," *Physical Review*, vol. 113, no. 1, pp. 273–279, 1959.
- [7] H. Kwon, F. Boehm, A. A. Hahn et al., "Search for neutrino oscillations at a fission reactor," *Physical Review D*, vol. 24, no. 5, pp. 1097–1111, 1981.
- [8] Y. Declais, R. Aleksan, M. Avenier et al., "Search for neutrino oscillations at 15, 40 and 95 meters from a nuclear power reactor at Bugey," *Nuclear Physics B*, vol. 434, no. 3, pp. 503–532, 1995.
- [9] G. Zacek, F. V. Feilitzsch, R. L. Mössbauer et al., "Neutrino-oscillation experiments at the Gösigen nuclear power reactor," *Physical Review D*, vol. 34, no. 9, pp. 2621–2636, 1986.
- [10] Y. Declais, H. de Kerret, B. Lefèvre et al., "Study of reactor antineutrino interaction with proton at Bugey nuclear power plant," *Physics Letters B*, vol. 338, no. 2-3, pp. 383–389, 1994.
- [11] A. Afonin et al., *JETP Letters*, vol. 93, p. 1, 1988.
- [12] G. S. Vidyakin, V. N. Vyrodov, Yu. V. Kozlov et al., "Limitations on the characteristics of neutrino oscillations," *JETP Letters*, vol. 59, pp. 390–393, 1994.
- [13] G. Vidyakin et al., *JETP Letters*, vol. 93, p. 424, 1987.
- [14] G. Vidyakin et al., *JETP Letters*, vol. 59, p. 390, 1994.
- [15] Z. Greenwood, W. R. Kropp, M. A. Mandelkern et al., "Results of a two-position reactor neutrino-oscillation experiment," *Physical Review D*, vol. 53, no. 11, pp. 6054–6064, 1996.
- [16] F. Ardellier, I. Barabanov, J. C. Barriere et al., "Double chooz, a search for the neutrino mixing angle theta-13," <http://arxiv.org/abs/hepex/060602>.
- [17] X. Guo, N. Wang, R. Wang et al., "A precision measurement of the neutrino mixing angle theta-13 using reactor Antineutrinos at Daya Bay," <http://arxiv.org/abs/hep-ex/0701029>.
- [18] J. Ahn and Reno Collaboration, "RENO: an experiment for neutrino oscillation parameter theta-13 using reactor neutrinos at Yonggwang," <http://arxiv.org/abs/1003.1391>.
- [19] K. Schreckenbach, G. Colvin, W. Gelletly, and F. von Feilitzsch, "Determination of the antineutrino spectrum from ^{235}U thermal neutron fission products up to 9.5 MeV," *Physics Letters B*, vol. 160, no. 4-5, pp. 325–330, 1985.
- [20] F. von Feilitzsch, A. A. Hahn, and K. Schreckenbach, "Experimental beta-spectra from ^{239}Pu and ^{235}U thermal neutron fission products and their correlated antineutrino spectra," *Physics Letters B*, vol. 118, no. 1-3, pp. 162–166, 1982.
- [21] A. Hahn, K. Schreckenbach, W. Gelletly, F. von Feilitzsch, G. Colvin, and B. Krusche, "Antineutrino spectra from ^{241}Pu and ^{239}Pu thermal neutron fission products," *Physics Letters B*, vol. 218, no. 3, pp. 365–368, 1989.
- [22] Th. Mueller, D. Lhuillier, M. Fallot et al., "Improved predictions of reactor antineutrino spectra," *Physical Review C*, vol. 83, no. 5, Article ID 054615, 17 pages, 2011.
- [23] W. Mampe, K. Schreckenbach, P. Jeuch et al., "The double focusing iron-core electron-spectrometer "BILL" for high resolution (n, e^-) measurements at the high flux reactor in Grenoble," *Nuclear Instruments and Methods*, vol. 154, no. 1, pp. 127–149, 1978.
- [24] A. Sirlin, "General properties of the electromagnetic corrections to the beta decay of a physical nucleon," *Physical Review*, vol. 164, no. 5, pp. 1767–1775, 1967.
- [25] P. Vogel, "Analysis of the antineutrino capture on protons," *Physical Review D*, vol. 29, no. 9, pp. 1918–1922, 1984.
- [26] J. Hardy, B. Jonson, and P. G. Hansen, "A comment on Pandemonium," *Physics Letters B*, vol. 136, no. 5-6, pp. 331–333, 1984.
- [27] <http://www.nndc.bnl.gov/ensdf>.
- [28] O. Tengblad, K. Aleklett, R. von Dincklage, E. Lund, G. Nyman, and G. Rudstam, "Integral gn-spectra derived from experimental β -spectra of individual fission products," *Nuclear Physics A*, vol. 503, no. 1, pp. 136–160, 1989.

- [29] R. Greenwood, R. G. Helmer, M. A. Lee et al., "Total absorption gamma-ray spectrometer for measurement of beta-decay intensity distributions for fission product radionuclides," *Nuclear Instruments and Methods in Physics Research A*, vol. 314, no. 3, pp. 514–540, 1992.
- [30] O. Meplan, in *Proceeding of the European Nuclear Conference. Nuclear Power for the 21st Century: From Basic Research to High-Tech Industry*, Versailles, France, 2005.
- [31] P. Vogel, "Conversion of electron spectrum associated with fission into the antineutrino spectrum," *Physical Review C*, vol. 76, no. 2, Article ID 025504, 5 pages, 2007.
- [32] P. Huber, "Determination of antineutrino spectra from nuclear reactors," *Physical Review C*, vol. 84, no. 2, Article ID 024617, 16 pages, 2011, Erratum-ibid. vol. 85, Article ID 029901, 2012.
- [33] D. Lhuillier, *Recent re-evaluation of reactor neutrino fluxes, slides of a talk given at Sterile Neutrinos at the Crossroads*, Blacksburg, Va, USA, 2011.
- [34] N. H. Haag, private communication, 2004.
- [35] J. Katakura et al., "JENDL Fission Product Decay Data File," 2000.
- [36] K. Takahashi, "Gross theory of first forbidden β -decay," *Progress of Theoretical Physics*, vol. 45, no. 5, pp. 1466–1492, 1971.
- [37] P. Vogel, G. K. Schenter, F. M. Mann, and R. E. Schenter, "Reactor antineutrino spectra and their application to antineutrino-induced reactions. II," *Physical Review C*, vol. 24, no. 4, pp. 1543–1553, 1981.
- [38] B. Pontecorvo, "Inverse beta processes and nonconservation of lepton charge," *Zhurnal Eksperimentalnoi i Teoreticheskoi Fiziki*, vol. 34, p. 247, 1958.
- [39] B. Pontecorvo, "Inverse beta processes and nonconservation of lepton charge," *Soviet Physics, JETP*, vol. 7, pp. 172–173, 1958.
- [40] Z. Maki, M. Nakagawa, and S. Sakata, "Remarks on the unified model of elementary particles," *Progress of Theoretical Physics*, vol. 28, no. 5, pp. 870–880, 1962.
- [41] M. Apollonio, A. Baldinib, C. Bemporad et al., "Limits on neutrino oscillations from the CHOOZ experiment," *Physics Letters B*, vol. 466, no. 2–4, pp. 415–430, 1999.
- [42] M. Apollonio, A. Baldini, C. Bemporad et al., "Search for neutrino oscillations on a long base-line at the CHOOZ nuclear power station," *The European Physical Journal C*, vol. 27, pp. 331–374, 2003.
- [43] A. Gando, Y. Gando, K. Ichimura et al., "Constraints on θ_{13} from a three-flavor oscillation analysis of reactor antineutrinos at KamLAND," *Physical Review D*, vol. 83, no. 5, Article ID 052002, 11 pages, 2011.
- [44] P. Adamson, C. Andreopoulos, D. J. Auty et al., "New constraints on muon-neutrino to electron-neutrino transitions in MINOS," *Physical Review D*, vol. 82, Article ID 051102, 6 pages, 2010.
- [45] K. Abe, N. Abgrall, Y. Ajima et al., "Indication of electron neutrino appearance from an accelerator-produced off-axis Muon neutrino beam," *Physical Review Letters*, vol. 107, no. 4, Article ID 041801, 8 pages, 2011.
- [46] P. Adamson, D. J. Auty, D. S. Ayres et al., "Improved search for Muon-neutrino to electron-neutrino oscillations in MINOS," *Physical Review Letters*, vol. 107, no. 18, Article ID 181802, 6 pages, 2011.
- [47] Y. Abe, C. Aberle, T. Akiri et al., "Indication of reactor $\bar{\nu}_e$ disappearance in the double chooz experiment," *Physical Review Letters*, vol. 108, no. 13, Article ID 131801, 7 pages, 2012.
- [48] Y. Abe, C. Aberle, J. C. dos Anjos et al., "Reactor electron antineutrino disappearance in the Double Chooz experiment," *Physical Review D*, vol. 86, no. 5, Article ID 052008, 21 pages, 2012.
- [49] G. L. Fogli, E. Lisi, A. Marrone, A. Palazzo, and A. M. Rotunno, "Evidence of $\theta_{13} > 0$ from global neutrino data analysis," *Physical Review D*, vol. 84, no. 5, Article ID 053007, 7 pages, 2011.
- [50] T. Schwetz, M. Tórtola, and J. W. F. Valle, "Where we are on θ_{13} : addendum to 'Global neutrino data and recent reactor fluxes: status of three-flavor oscillation parameters,'" *New Journal of Physics*, vol. 13, Article ID 109401, 5 pages, 2011.
- [51] F. P. An, J. Z. Bai, A. B. Balantekin et al., "Observation of electron-antineutrino disappearance at daya bay," *Physical Review Letters*, vol. 108, Article ID 171803, 7 pages, 2012.
- [52] J. K. Ahn, S. Chebotaryov, J. H. Choi et al., "Observation of reactor electron antineutrinos disappearance in the RENO experiment," *Physical Review Letters*, vol. 108, no. 19, Article ID 191802, 6 pages, 2012.
- [53] F. P. An and Daya Bay Collaboration, "Improved measurement of electron antineutrino disappearance at Daya Bay," *Chin. Phys. C* 37(2013) 011001.
- [54] F. P. An, Q. Anb, J. Z. Bai et al., "A side-by-side comparison of Daya Bay antineutrino detectors," *Nuclear Instruments and Methods in Physics Research A*, vol. 685, pp. 78–97, 2012.
- [55] <http://www.cgnpc.com.cn/n1093/n463576/n463598/>.
- [56] Y. Y. Ding, Z. Y. Zhang, P. J. Zhou, J. C. Liu, Z. M. Wang, and Y. L. Zhao, "Research and development of gadolinium loaded liquid scintillator for Daya Bay neutrino experiment," *Journal of Rare Earths*, vol. 25, pp. 310–313, 2007.
- [57] Y. Y. Ding, Z. Zhang, J. Liu, Z. Wang, P. Zhou, and Y. Zhao, "A new gadolinium-loaded liquid scintillator for reactor neutrino detection," *Nuclear Instruments and Methods in Physics Research A*, vol. 584, no. 1, pp. 238–243, 2008.
- [58] M. Yeh, A. Garnov, and R. L. Hahn, "Gadolinium-loaded liquid scintillator for high-precision measurements of antineutrino oscillations and the mixing angle, θ_{13} ," *Nuclear Instruments and Methods in Physics Research A*, vol. 578, no. 1, pp. 329–339, 2007.
- [59] Q. Zhang, Y. Wang, J. Zhang et al., "An underground cosmic-ray detector made of RPC," *Nuclear Instruments and Methods in Physics Research A*, vol. 583, no. 2–3, pp. 278–284, 2007, Erratum-ibid. A, vol. 586, p. 374, 2008.
- [60] <http://geant4.cern.ch/>.
- [61] L. J. Wen, J. Cao, K.-B. Luk, Y. Ma, Y. Wang, and C. Yang, "Measuring cosmogenic ^9Li background in a reactor neutrino experiment," *Nuclear Instruments and Methods in Physics Research A*, vol. 564, no. 1, pp. 471–474, 2006.
- [62] T. Nakagawa, K. Shibata, S. Chiba et al., "Japanese evaluated nuclear data library version 3 revision-2: JENDL-3.2," *Journal of Nuclear Science and Technology*, vol. 32, no. 12, pp. 1259–1271, 1995.
- [63] J. Cao, "Determining reactor neutrino flux," *Nuclear Physics B—Proceedings Supplements*. In press, <http://arxiv.org/abs/1101.2266>, Proceeding of Neutrino 2010.
- [64] S. F. E. Tournu et al., Tech. Rep. EPRI 2001.1001470, Palo Alto, Calif, USA, 2001.
- [65] C. Xu, X. N. Song, L. M. Chen, and K. Yang, *Chinese Journal of Nuclear Science and Engineering*, vol. 23, p. 26, 2003.
- [66] S. Rauck, "SCIENCE V2 nuclear code package—qualification report (Rev A)," Framatome ANP Document NFPSP/DC/89, 14, 2004.
- [67] R. Sanchez, I. Zmijarevi, M. Coste-Delclaux et al., "APOLLO2 YEAR 2010," *Nuclear Engineering and Technology*, vol. 42, no. 5, pp. 474–499, 2010.

- [68] R. R. G. Marleau, A. Hebert, and R. Roy, "A user guide for DRAGON," Tech. Rep. IGE-236 Rev. 1, 2001.
- [69] C. E. Sanders and I. C. Gauld, "ORNL, isotopic analysis of high-burnup PWR spent fuel samples from the takahama-3 reactor," Tech. Rep. NUREG/CR-6798, ORNL/TM-2001/259, 2002.
- [70] Z. Djurcic, J. A. Detwiler, A. Piepke, V. R. Foster, L. Miller, and G. Gratta, "Uncertainties in the anti-neutrino production at nuclear reactors," *Journal of Physics G*, vol. 36, no. 4, Article ID 045002, 2009.
- [71] P. Vogel and J. F. Beacom, "Angular distribution of neutron inverse beta decay, $\bar{\nu}_e + \bar{p}e^+ + n$," *Physical Review D*, vol. 60, no. 5, Article ID 053003, 10 pages, 1999.
- [72] V. I. Kopeikin, L. A. Mikaelyan, and V. V. Sinev, "Reactor as a source of antineutrinos: thermal fission energy," *Physics of Atomic Nuclei*, vol. 67, no. 10, pp. 1892–1899, 2004.
- [73] F. P. An, G. Jie, Z. Xiong-Wei, and L. Da-Zhang, "Simulation study of electron injection into plasma wake fields by colliding laser pulses using OOPIC," *Chinese Physics C*, vol. 33, article 711, 2009.
- [74] B. Zhou, R. Xi-Chao, N. Yang-Bo, Z. Zu-Ying, A. Feng-Peng, and C. Jun, "A study of antineutrino spectra from spent nuclear fuel at Daya Bay," *Chinese Physics C*, vol. 36, no. 1, article 001, 2012.
- [75] D. Stump, J. Pumplin, R. Brock et al., "Uncertainties of predictions from parton distribution functions. I. The Lagrange multiplier method," *Physical Review D*, vol. 65, no. 1, Article ID 014012, 17 pages, 2001.
- [76] NEA-1845/01, documentation for MURE, 2009.
- [77] G. Marleau et al., Tech. Rep. IGE-157, 1994.
- [78] C. Jones, *Prediction of the reactor antineutrino flux for the double chooz experiment [Ph.D. thesis]*, MIT, Cambridge, Mass, USA, 2012.
- [79] C. Jones, A. Bernstein, J. M. Conrad et al., "Reactor simulation for antineutrino experiments using DRAGON and MURE," <http://arxiv.org/abs/1109.5379>.
- [80] A. Pichlmaier, V. Varlamov, K. Schreckenbach, and P. Geltenbort, "Neutron lifetime measurement with the UCN trap-in-trap MAMBO II," *Physics Letters B*, vol. 693, no. 3, pp. 221–226, 2010.
- [81] J. Allison, K. Amako, J. Apostolakis et al., "Geant4 developments and applications," *IEEE Transactions on Nuclear Science*, vol. 53, no. 1, pp. 270–278, 2006.
- [82] J. S. Agostinelli, J. Allison, K. Amako et al., "Geant4—a simulation toolkit," *Nuclear Instruments and Methods in Physics Research A*, vol. 506, no. 3, pp. 250–303, 2003.
- [83] D. R. Tilley, J. H. Kelley, J. L. Godwin et al., "Energy levels of light nuclei $A = 8, 9, 10$," *Nuclear Physics A*, vol. 745, no. 3–4, pp. 155–362, 2004.
- [84] Y. Prezado, M. J. G. Borge, C. A. Diget et al., "Low-lying resonance states in the ^9Be continuum," *Physics Letters B*, vol. 618, no. 1–4, pp. 43–50, 2005.
- [85] P. Papka, T. A. D. Brown, B. R. Fulton et al., "Decay path measurements for the 2.429 MeV state in ^9Be : implications for the astrophysical $\alpha + \alpha + n$ reaction," *Physical Review C*, vol. 75, no. 4, Article ID 045803, 8 pages, 2007.
- [86] <http://www.chem.agilent.com/en-US/Products/instruments/molecularspectroscopy/fluorescence/systems/caryclipse/pages/default.aspx>.
- [87] C. Aberle, C. Buck, B. Gramlich et al., "Large scale Gd-beta-diketonate based organic liquid scintillator production for anti-neutrino detection," *Journal of Instrumentation*, vol. 7, Article ID P06008, 2012.
- [88] C. Aberle, C. Buck, F. X. Hartmann, S. Schönert, and S. Wagner, "Light output of Double Chooz scintillators for low energy electrons," *Journal of Instrumentation*, vol. 6, Article ID P11006, 2011.
- [89] C. Aberle, [Ph.D. thesis], Universität Heidelberg, Heidelberg, Germany, 2011.
- [90] P. Adamson, C. Andreopoulos, R. Armstrong et al., "Measurement of the neutrino mass splitting and flavor mixing by MINOS," *Physical Review Letters*, vol. 106, no. 18, Article ID 181801, 6 pages, 2011.
- [91] H. Nunokawa, S. Parke, and R. Z. Funchal, "Another possible way to determine the neutrino mass hierarchy," *Physical Review D*, vol. 72, no. 1, Article ID 013009, 6 pages, 2005.
- [92] G. Feldman and R. Cousins, "Unified approach to the classical statistical analysis of small signals," *Physical Review D*, vol. 57, no. 7, pp. 3873–3889, 1998.
- [93] G. Mention, M. Fechner, Th. Lasserre et al., "Reactor antineutrino anomaly," *Physical Review D*, vol. 83, no. 7, Article ID 073006, 20 pages, 2011.
- [94] A. Hoummada and S. Lazrak Mikou, "Neutrino oscillations I.L.L. experiment reanalysis," *Applied Radiation and Isotopes*, vol. 46, no. 6–7, pp. 449–450, 1995.
- [95] P. Anselmann, R. Fockenbrocka, W. Hampel et al., "First results from the ^{51}Cr neutrino source experiment with the GALLEX detector," *Physics Letters B*, vol. 342, no. 1–4, pp. 440–450, 1995.
- [96] W. Hampel, G. Heusser, J. Kiko et al., "Final results of the ^{51}Cr neutrino source experiments in GALLEX," *Physics Letters B*, vol. 420, no. 1–2, pp. 114–126, 1998.
- [97] F. Kaether, W. Hampel, G. Heusser, J. Kiko, and T. Kirsten, "Reanalysis of the Gallex solar neutrino flux and source experiments," *Physics Letters B*, vol. 685, no. 2, pp. 47–54, 2010.
- [98] D. Abdurashitov, V. N. Gavrin, S. V. Girin et al., "The Russian-American gallium experiment (SAGE) Cr neutrino source measurement," *Physical Review Letters*, vol. 77, no. 23, pp. 4708–4711, 1996.
- [99] D. Abdurashitov, V. N. Gavrin, S. V. Girin et al., "Measurement of the response of a Ga solar neutrino experiment to neutrinos from a ^{37}Ar source," *Physical Review C*, vol. 73, no. 4, Article ID 045805, 12 pages, 2006.
- [100] D. Abdurashitov, V. N. Gavrin, V. V. Gorbachev et al., "Measurement of the solar neutrino capture rate with gallium metal. III. Results for the 2002–2007 data-taking period," *Physical Review C*, vol. 80, no. 1, Article ID 015807, 16 pages, 2009.
- [101] C. Giunti and M. Laveder, "Short-baseline electron neutrino disappearance, tritium beta decay, and neutrinoless double-beta decay," *Physical Review D*, vol. 82, no. 5, Article ID 053005, 14 pages, 2010.
- [102] A. Bernstein, in *Proceedings of Neutrinos and Arm Control Workshop*, Honolulu, Hawaii, USA, 2003.
- [103] A. Porta et al., "Reactor neutrino detection for non proliferation with the Nucifer experiment," *Journal of Physics: Conference Series*, vol. 203, no. 1, Article ID 012092, 2010.
- [104] S. T. Petcov and M. Piai, "The LMA MSW solution of the solar neutrino problem, inverted neutrino mass hierarchy and reactor neutrino experiments," *Physics Letters B*, vol. 533, no. 1–2, pp. 94–106, 2002.
- [105] S. Choubey, S. T. Petcov, and M. Piai, "Precision neutrino oscillation physics with an intermediate baseline reactor neutrino experiment," *Physical Review D*, vol. 68, no. 11, Article ID 113006, 19 pages, 2003.

- [106] J. Learned, S. T. Dye, S. Pakvasa, and R. C. Svoboda, "Determination of neutrino mass hierarchy and θ_{13} with a remote detector of reactor antineutrinos," *Physical Review D*, vol. 78, no. 7, Article ID 071302, 5 pages, 2008.
- [107] L. Zhan, Y. Wang, J. Cao, and L. Wen, "Determination of the neutrino mass hierarchy at an intermediate baseline," *Physical Review D*, vol. 78, no. 11, Article ID 111103, 5 pages, 2008.
- [108] L. Zhan, Y. Wang, J. Cao, and L. Wen, "Experimental requirements to determine the neutrino mass hierarchy using reactor neutrinos," *Physical Review D*, vol. 79, no. 7, Article ID 073007, 5 pages, 2009.
- [109] S. B. Kim, in *Talk Given at the Conference of Neutrino*, 2012.
- [110] J. Beringer, J.-F. Arguin, R. M. Barnett et al., "Review of particle physics," *Physical Review D*, vol. 86, no. 1, Article ID 010001, 1528 pages, 2012.

